Pure Appl. Geophys. 180 (2023), 1489–1520

https://doi.org/10.1007/s00024-022-03134-5

Pure and Applied Geophysics

Impact of Environmental Backgrounds on Atmospheric Monitoring of Nuclear Explosions

Paul W. Eslinger,[1] Harry S. Miley,[1] Christine M. Johnson,[1] Ramesh S. Sarathi,[1] and Brian T. Schrom[1]

Abstract—Radionuclide monitoring for nuclear explosions includes measuring radioactive aerosol and noble gas concentrations in the atmosphere. The International Monitoring System (IMS) of the Comprehensive Nuclear Test-Ban Treaty has made such measurements for decades, revealing much about how atmospheric radioactivity impacts the sensitivity of the network. For example, civilian emissions of radioiodine make a substantial regional impact, but a minor global impact, while civilian radioxenon emissions create major regional and complex global impacts. The impacts are strongly influenced by the minimum releases anticipated to be interesting. The original design of the IMS anticipated relatively large releases, and the current IMS network substantially meets or exceeds the sensitivity needed to detect those levels. Much lower signal levels can be motivated from historical tests. Using a release that corresponds roughly to a one-ton equivalent of fission in the atmosphere rather than the design level of one-kiloton equivalent, the network detection probabilities for ^{140}Ba and ^{131}I are quite good ($\sim$ 75%) and for ^{133}Xe is still considerable ($\sim$ 45%). Using measured and simulated background concentrations, various possible desired signal levels, and an innovative anomaly threshold, maps of sensitivity and a station ranking are developed for IMS radionuclide stations. These provide a strong motivation for additional experimentation to learn about sources and the potential plusses of new technology.

Keywords: International monitoring system, nuclear explosion, treaty verification, atmospheric transport modeling, network design.

1. Introduction

Several phenomena created by nuclear explosions can be used to remotely monitor for their occurrence (Maceira et al., 2017). The International Monitoring System (IMS) (CTBTO PrepCom, 2019) is composed of seismic, hydroacoustic, infrasound, and radionuclide (RN) networks that monitor the earth for events that would violate the Comprehensive Nuclear-Test-Ban Treaty (1996).

Industrial activities, such as medical isotope production facilities, nuclear research reactors, and nuclear power reactors, also release radioactive materials to the atmosphere. Quantifying the impact of these anthropogenic backgrounds of ^{140}Ba, ^{131}I, and ^{133}Xe on IMS radionuclide stations is a major goal of this work.

The historical design-basis studies in working paper WP.224 (IMS Expert Group, 1995) considered 50-, 75-, and 100-station networks for ^{140}Ba and also a 100-station network for ^{133}Xe, with a caveat that there was insufficient time to evaluate 50- and 75-station ^{133}Xe networks. The CTBT calls for 80 RN stations, but one of the 80 was not assigned coordinates. Also, noble gas samplers are planned for 40 stations, although the possibility exists to install them at additional RN locations after the treaty goes into force. Therefore, the noble gas results provided here consider both 39- and 79-station networks, using the coordinates defined in the text of the Treaty.

The WP.224 aerosol detection design goal is > 90% probability of detecting a 1 kiloton TNT equivalent atmospheric nuclear test within 10 days (Schulze et al., 2000) using the isotope ^{140}Ba. While nuclear fission of actinides creates many radioactive isotopes, ^{140}Ba is considered a top signature because of its high fission yield, favorable decay scheme, and moderate half-life which facilitates detection at global scales.

1.1. Isotopes Released from Historical Nuclear Tests

Radioactive xenon is an important indicator used in detecting underground nuclear explosions, as noble gases are by far the most likely to leak through

[1] Pacific Northwest National Laboratory, 902 Battelle Blvd., Richland, WA 99354, USA. E-mail: paul.w.eslinger@pnnl.gov; harry.miley@pnnl.gov; christine.johnson@pnnl.gov; ramesh.sarathi@pnnl.gov; brian.schrom@pnnl.gov

geologic or engineered containment. Dubasov (2010) recorded xenon detections for over 40% of underground nuclear explosive tests conducted at Semipalatinsk, for example. By comparison, many aerosol isotopes are generated in a nuclear explosion, but only a few have been observed at the surface from underground nuclear explosions.

Isotopes useful for monitoring should have half-lives long enough to allow the isotope to travel 1000 km or further downwind before it decays below detectable levels, but not so long that it does not register many decays in a measurement period. Likewise, the fission yield should be as high as possible to increase detection probabilities. As will be shown in Sec. 2.1, in the case of ^{133}Xe, the maximum inventory is reached about 3 days after the fission occurs if ^{133}I is held together with the xenon.

Both ^{133}Xe and ^{135}Xe were frequently observed leaking from U.S. underground nuclear explosive tests (Schoengold et al., 1996). Due to their relatively large yields and inert nature, ^{135}Xe is much less likely to be detected far from the release location because of its relatively short half-life. The number of times selected isotopes were observed leaking from U.S. underground explosive tests (Schoengold et al., 1996) are tabulated in Table 1 along with their half-life and fission yield. The IMS noble gas network frequently detects ^{133}Xe but rarely detects other xenon isotopes despite their release by nuclear power plants and medical isotope production facilities.

Next-generation noble gas systems have just been being deployed (Ringbom et al., 2017) in the IMS or are nearing the completion of pre-deployment tests (Chernov et al., 2021; Hayes et al., 2013; TBE, 2020; Topin et al., 2020). These systems will have better detection thresholds for all xenon isotopes and may result in more detections from background sources.

Molybdenum, barium, and lanthanum are considered 'refractory,' i.e., non-volatile, however, barium and lanthanum isotopes have short-lived xenon precursors, ^{139}Xe ($T_{1/2}$ = 39.7 s) and ^{140}Xe ($T_{1/2}$ = 13.6 s). Perhaps the ^{140}Ba and ^{140}La entries in Table 1 are observed with a greater frequency than ^{99}Mo because of very prompt leaks of ^{139}Xe and ^{140}Xe rather than direct emission of the refractory particles.

In Table 1, the frequency of detections at U.S. underground nuclear explosive tests are listed, but this frequency is without regard for the relative sensitivity of measurement systems employed. Systems in the IMS today have noble gas sensitivities in the 0.2–0.5 milli Becquerel per cubic meter (mBq/m^3) range, while aerosol systems have sensitivities around 10 μBq/m^3. This is because the aerosol minimum detectable concentration (MDC) formula depends (Miley et al., 2019) on the inverse square root of the sampled volume, which for an aerosol system is as much as a thousand times larger than a xenon system, but still using less power than that needed to remove tens of cubic centimeters of xenon

Table 1

Frequency of detection by isotope for the 824 underground nuclear explosive tests conducted in Nevada (Schoengold et al., 1996)

Noble gas				Volatile above 600 °C				Refractory			
Isotope	Number	$T_{1/2}$	Cum. yield	Isotope	Number	$T_{1/2}$	Cum. yield	Isotope	Number	$T_{1/2}$	Cum. yield
^{131m}Xe	10	11.8 d	0.0451	^{131}I	131	8.03 d	3.22	^{99}Mo	3	65.9 h	5.94
^{133}Xe	310	5.25 d	6.72	^{132}I	13	2.30 h	4.67	^{99m}Tc	1	6.01 h	5.23
^{133m}Xe	169	2.20 d	0.192	^{133}I	109	20.8 h	6.72	^{139}Ba	6	82.9 m	6.34
^{135}Xe	271	9.14 h	6.60	^{134}I	6	52.5 m	7.64	^{140}Ba	19	12.8 d	5.98
				^{135}I	88	6.58 h	6.30	^{140}La	17	1.68 d	5.98
				^{132}Te	13	3.20 d	4.66				
				^{137}Cs	10	30.1 y	6.22				
				^{138}Cs	29	32.5 m	6.65				
				^{139}Cs	1	9.27 m	6.32				

The cumulative yield for each isotope (number of atoms per 100 fissions) are from the fast fission of ^{235}U published by England and Rider (1994). Releases listed as 'accidental' comprised about 50% of these ^{131}I releases

from tens of cubic meters of air. Thus, it is possible that the reported ratio of xenon to aerosol detections in Schoengold et al. (1996) are skewed toward aerosol detections by a factor of 20 or more. In any case, for underground test leakage, the three iodine isotopes ^{131}I, ^{133}I, and ^{135}I were detected far more often than the aerosol isotopes ^{99}Mo and ^{140}Ba that are favored for a direct release of fission products to the atmosphere.

1.2. Types of Background Radionuclide Signals

Like many measurement systems, IMS radionuclide measurement systems must contend with background signals. These can come in two varieties and are dealt with quite differently. First, there is natural radioactivity in Earth's atmosphere. For aerosol systems, radon decay products such as ^{212}Pb, ^{212}Bi, and ^{208}Tl collected on the sample provide a background of Compton scattered gamma ray signals across a wide spectral energy range, obscuring the gamma ray signals below 2615 keV. These background signals increase the MDC of ^{140}Ba, ^{131}I, and all other aerosol isotopes of interest, because the gamma ray signals from the isotopes of interest must significantly exceed fluctuations in the background signals to be registered. Because these decay products originate from radon upwelling in continents, their signals are stronger at interior continental locations than at coastal locations, which are in turn stronger than at island locations. The daily ^{212}Pb concentrations at RN79 (Oahu, Hawaii, USA) and RN70 (Sacramento, California, USA) shown in Fig. 1 illustrate the large variation in ^{212}Pb background concentrations. As seen in Fig. 1, there are also significant seasonal variations at many locations. The ^{140}Ba MDC values for the network vary from 3.1 to 23.2 μBq/m^3 as shown in Table 9 in the appendix and corresponding MDC fluctuations would occur in all other isotopes. Aerosol removal due to rain and radon variation due to barometric pressure changes add an additional element of variability to these signals. In xenon measurement systems, variations in radon can likewise impact the spectra results, but filtration, chemical separation, and energy spectrum analysis are employed to greatly minimize this effect.

A second type of background occurs when activities unrelated to nuclear explosions release the same isotopes of interest. Nuclear power plants (Kalinowski & Tatlisu, 2020; Kalinowski & Tuma, 2009) and medical isotope production facilities (Bowyer et al., 2013; Saey, 2009; Saey et al., 2010a, 2010b; Stocki et al., 2008; Wotawa et al., 2010) and nuclear research facilities (Hoffman & Berg, 2018) also release the same xenon isotopes to the environment as a nuclear explosion. Each of these sources of fission products has an associated leakage rate and have been studied in relation to IMS signals (Achim et al., 2016; Gueibe et al., 2017; Schoeppner & Plastino, 2014). Figure 2 shows the monitoring locations in the IMS, the locations of 181 active nuclear power production facilities, and the locations

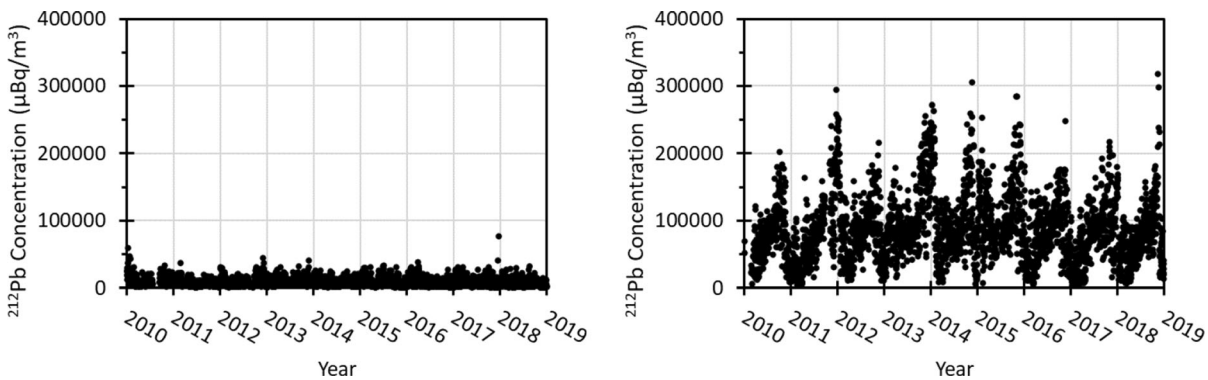

Figure 1
Daily ^{212}Pb concentrations for 9 years at RN79 (Oahu, Hawaii, USA) (left panel) and RN70 (Sacramento, California, USA) (right panel). The same vertical scale is used on both graphs to emphasize the large variation of values at different locations

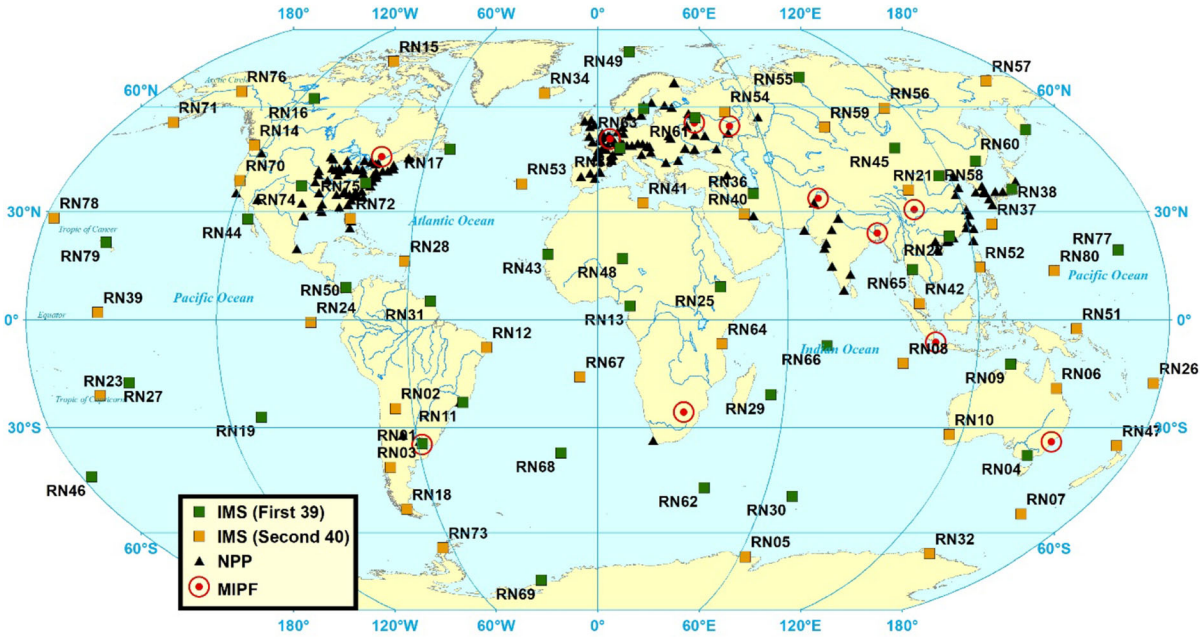

Figure 2
Map of IMS radionuclide monitoring locations, nuclear power reactors, and medical isotope production facilities

of the 11 largest fission-based producers of medical isotopes. The facile assumption that nearby IMS stations suffer the most from anthropogenic backgrounds is generally true but quantifying the impact on both nearby and distant stations is challenging and a major goal of this work.

2. Methods and Data

To study the impact of background radioactivity on a network of RN sensors, the network design, sensor sensitivity, and the intended source term must be considered. In this study, we take as a given the 79 locations for radionuclide monitoring in the IMS and the sensitivity of currently deployed IMS systems. These will be considered versus a wide range of source strength intended to explore the entire range of network response. Rather than a simple formula for detection sensitivity, the authors also employ a frequency-based approach for some backgrounds, such that an anomaly or action threshold is achieved at the 95th percentile of frequently seen backgrounds. In the future, as the natural backgrounds and many anthropogenic backgrounds become sufficiently well-known and, on average, predictable, studies could be done to predict the performance of different networks, different sensors, and different detection criteria.

2.1. Source Terms for Network Detection Analyses

The original IMS design document, WP.224 (IMS Expert Group, 1995), identified the magnitude of the aerosol source term M = 2×10^{15} Bq of ^{140}Ba and presented the rationale that this activity corresponds to lofting 90% of the fission products from a 1 kiloton fission explosion in the atmosphere. As seen in Table 1, ^{131}I is far more likely to be released from a nuclear explosion contained underground than other aerosol species. Despite the original thought of a network of aerosol samplers developed to detect radioactive releases from an atmospheric nuclear explosive test, this study will consider the utility of ^{131}I leakage from underground nuclear explosive tests. Compared to ^{140}Ba, this isotope also has a high fission yield (3%), a favorable decay scheme for gamma ray spectroscopy, and a useful half-life of

8.24 days. There have been a number of ^{131}I detections in the IMS, presumably from the production and use of medical isotopes, so it is conceivable that backgrounds could hamper the use of the isotope for detecting underground nuclear explosive tests. Other fission and activation products (e.g., legacy ^{137}Cs and cosmogenic ^{24}Na) are frequently detected by the IMS, but because of the importance of iodine releases from U.S. underground nuclear explosive tests, the authors will use ^{131}I to explore the impact of aerosol backgrounds.

The xenon source term in WP.224 is differentiated between a ^{133}Xe source magnitude of 10^{15} Bq for 'evasive atmospheric tests', where rain eliminates aerosols, but 90% of instantaneous xenon isotopes are lofted, 10^{15} Bq of instantaneous release for underwater nuclear explosions, and 10^{14} Bq released over 12 h, or 10% of the xenon, for a 1 kiloton underground nuclear explosion. The release timing is important, because the radioactive precursor to xenon is iodine, which is less likely to escape from underwater or underground explosions. The amount of ^{133}Xe as a function of time past a nuclear explosion with a 1 kiloton yield for cumulative xenon and iodine isotopes and fractionated ^{133}Xe is shown in Fig. 3. Isotopic inventories were generated using a combination of the MCNP6 code (Goorley et al., 2012) for estimation of neutron fluxes and the ORIGEN2.2 code (Croff, 1980) to calculate the resulting irradiation material balances from those fluxes. From the fractionated ^{133}Xe curve (lowest curve in the plots), it is evident that leakage of ^{133}Xe from a nuclear explosion during the earliest hours would be strongly suppressed due to the lack of ^{133}I ingrowth during later containment. The average from the cumulative ^{133}Xe curve during the earliest 12 h, as in WP.224, is 6×10^{14} Bq before loss of containment. The WP.224 estimate implies a 17% leakage of ^{133}Xe over this time.

To fully understand the range of responses of the 79-station network, it will be tested with a range of source strengths wide enough to determine where the network sensitivity begins, and where it maximizes. The source strengths used in this study run from 10^9 to 10^{16} Bq for the three isotopes mentioned above, ^{140}Ba, ^{131}I, and ^{133}Xe, such that this activity range corresponds to nuclear explosion yields in the atmosphere from 100 g to 1 kiloton.

2.2. *Minimum Detectable Concentrations and the Influence of ^{212}Pb*

The original IMS design document (IMS Expert Group, 1995) calls for an MDC of 10 μBq/m^3 for ^{140}Ba, achieved in a 3-day sampling period including collection and measurement. The MDC for aerosols

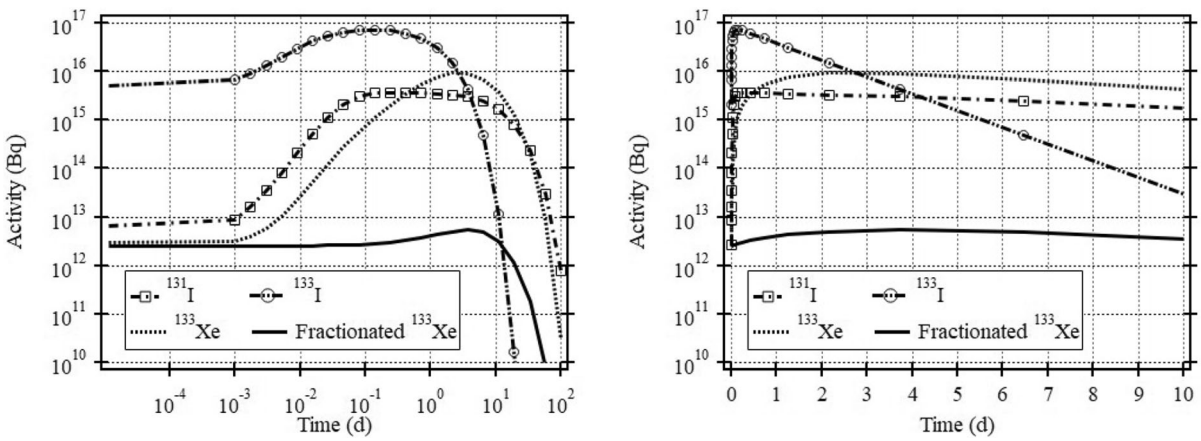

Figure 3
Comparison of some ^{235}U fission products from a one kiloton equivalent nuclear explosion: the initial independent quantity of ^{133}Xe, compared with the ingrowth and decay of ^{133}I cumulating into ^{133}Xe. Also, ^{131}I is shown. Note that ^{133m}Xe, not shown, also decays into ^{133}Xe. The log-time left panel illustrates the rapid growth of ^{133}Xe due to ^{133}I decay that is lost when the xenon is released (fractionated) at early time

depends on several factors related to the decay of background sources and of the analyte of interest, including the efficiency of the detector and the branching fraction of the isotope in a region of interest. The MDC equation (Miley et al., 2019) includes the square root of the observed count of background signals that occur in the region of interest for an isotope. This can be thought of as related to the uncertainty or fluctuation of the background signals. Many such MDC formulations could be created, but many use the statistical approach similar to that described by Currie (1968), in which a 5% false positive and 5% false negative choice is made. In general, the MDCs for different isotopes can differ greatly (a couple of orders of magnitude or more), and their response to different background concentrations can be different.

The concentration of ^{212}Pb is usually thought to be the main driver of background signals in IMS aerosol systems and varies widely from day to day and location to location. The MDCs of many analytes are calculated for each sample, but most of these are strongly impacted by ^{212}Pb. The IMS has gradually expanded since 2000 to include 72 of the 80 planned IMS stations. Sample measurement results include the MDC of ^{140}Ba and ^{131}I achieved in each measurement. A summary of the relevant historical MDC data for each station is provided in Appendix 1 for approximately 200,000 measured samples since the beginning of 2012, i.e., not including Fukushima-related measurements. The authors selected data from Reviewed Radionuclide Reports (RRR) that pass air flow-rate quality checks, acquisition time (counting) quality checks, and have a ^{212}Pb concentration of no more than 400,000 μBq/m^3. Information on the ^{212}Pb concentrations are included here because high ^{212}Pb concentrations can reduce the sensitivity of a detector (Werzi, 2010).

Setting target MDC values is useful when determining the ability of a sampling network to monitor for specific isotopes. However, after the target level was set and sampling systems were developed, the collected data showed that no sampler design can achieve the target MDC for ^{140}Ba of 10 μBq/m^3 in areas where the background levels of ^{212}Pb are extremely high. Thus, the definition of the target MDC level was revised to apply to the situation where no ^{212}Pb is present in the samples. A computational technique was then created to extract the performance the station would give with no ^{212}Pb. This approach uses groups of MDC values for an isotope (e.g., ^{131}I or ^{140}Be, etc.) and depends on the assumption that background counts originate from ^{212}Pb. The group of sample MDCs are fitted with a constant value, representing the radioactivity intrinsic to the system, and a term linear in the ^{212}Pb concentration. The following equation uses the ^{212}Pb concentrations, Pb_i, and the MDC values, MDC_i, from a group of samples (indexed by i):

$$MDC_i^2 = a + b \cdot Pb_i \tag{1}$$

where a and b are fitting constants obtained from a linear regression model.

Radionuclide Aerosol Sampler/Analyzer (RASA) systems (Miley et al., 1998) are deployed at 20 IMS radionuclide sampling stations. For aerosol sampler/analyzer systems, the concentrations and MDC have units of μBq/m^3. Using 3722 samples collected in 2019 at 11 RASA systems operated by the United States for the IMS, one obtains the following functional fits for ^{140}Ba and ^{131}I given the ^{212}Pb concentration, Pb, in each sample:

$$MDC_{Ba140} = \sqrt{72.32 + 0.02546 \cdot Pb} \tag{1a}$$

$$MDC_{I131} = \sqrt{8.86 + 0.03318 \cdot Pb} \tag{1b}$$

When the ^{212}Pb concentration is zero, MDC_{Ba140} = 8.50 and MDC_{I131} = 2.98 μBq/m^3 for these RASA systems.

The square of the sample MDC is plotted against the sample ^{212}Pb concentration in Fig. 4, showing that a linear fit is reasonable, and supports the assumption that ^{212}Pb and its decay products dominate background contributions to the MDC. But because the fitted line does not go through the origin, one can be certain that ^{212}Pb does not represent the entirety of the background signals.

As shown in Fig. 1, the ^{212}Pb concentrations vary from day to day, and also show seasonal fluctuations, thus the ^{140}Ba and ^{131}I MDCs also have daily and seasonal variations. An example of the range of MDCs is provided in Table 2 for 11 stations using RASA equipment. A station on Wake Island in the Pacific Ocean (RN77) has the smallest range. This

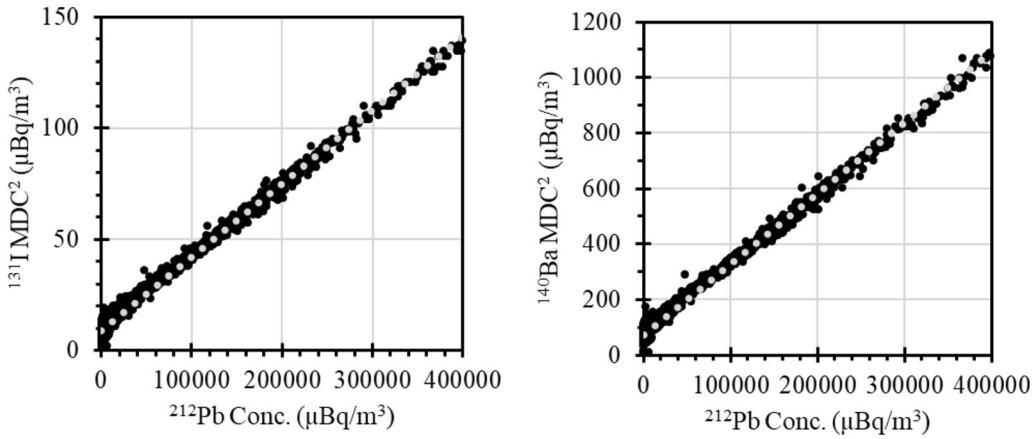

Figure 4
The square of measurement MDCs for ^{131}I (left pane) and ^{140}Ba (right pane) for 3,722 samples collected at 11 different RASA samplers in 2019 for a range of ^{212}Pb concentrations. The functional fits to adjust the MDC for varying levels of ^{212}Pb concentrations are shown by the dotted grey lines

Table 2

Sample MDC statistics for the ^{140}Ba MDC in μBq/m^3 for 2012 through 2020 at 11 stations operated by the United States for the International Monitoring System

Station	Location	Number samples	5% level	Average	95% level
RN70	Sacramento, CA	3206	12.4	17.1	22.6
RN71	Sand Point, AK	3165	6.43	7.9	10.6
RN72	Melbourne, FL	3090	8.23	9.3	11.0
RN73	Palmer Station, Antarctica	3165	8.19	9.6	10.7
RN74	Ashland, KS	3165	14.5	25.5	40.0
RN75	Charlottesville, VA	3043	11.6	17.5	25.5
RN76	Salchaket, AK	3225	10.2	11.9	13.5
RN77	Wake Island	3097	6.90	7.8	9.2
RN78	Midway Islands	3149	7.29	8.7	10.4
RN79	Oahu, HI	3152	8.70	9.9	11.4
RN80	Upi, Guam	3064	8.88	10.0	12.2

makes sense, because the ^{220}Rn that produces the ^{212}Pb mostly comes from atmospheric radon released from spontaneous fission of uranium and thorium in the surface rock. Of these 11 stations, the widest ^{212}Pb concentration range is found in RN74, which is located at Ashland, Kansas, near the center of North America.

After adjustment for background ^{212}Pb, the diverse group of IMS aerosol systems currently meet the target 10 μBq/m^3 MDC level for ^{140}Ba, although the lower ^{212}Pb background levels in some locations result in better (lower) MDCs. Data on the historical sample MDC values for ^{140}Ba and ^{131}I is provided in Table 9 in the Appendix for all IMS stations.

Three types of noble gas samplers are currently deployed in the IMS. The SAUNA (Ringbom et al., 2003) has a 0.2 mBq/m^3 MDC for ^{133}Xe using 12-h samples. The SPALAX (Fontaine et al., 2004) has a 0.15 mBq/m^3 MDC for ^{133}Xe using 24-h samples. The ARIX (Dubasov et al., 2005) has a 0.5 mBq/m^3 MDC for ^{133}Xe using 12-h samples. Information provided in Appendix 1 matches the sampler type with different sampling locations.

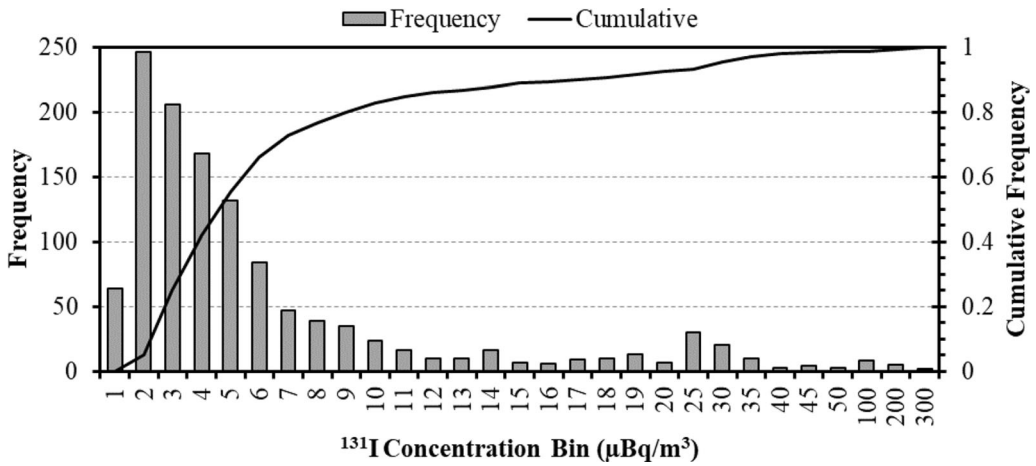

Figure 5
The frequency of ^{131}I detections as a function of concentration. Data are global and start in 2012, which is long enough after the Fukushima event that related ^{131}I will have decayed. The upper end of the horizontal axis (above 20 µBq/m^3) is not to scale

2.3. *Creating an Anomaly Level Using Historical Detections, and Applying to ^{131}I*

Above, the limitation that uninteresting radioactivity imposes on monitoring for atmospheric signatures was discussed for aerosol systems. The second perplexing source of monitoring interference is the appearance of the specific signatures of interest arising from uninteresting processes. An example of this can be seen from 2019 ^{133}Xe data from one station in Fig. 13 in the Appendix. This system collects and measures two samples a day with an MDC of about 0.2 mBq/m^3. The normalized integral of signals is also shown, such that by inspection it is clear that about 20%, or 150 reported signals are above the MDC of the system. If one assumes that there were no nuclear explosions in 2019, this distribution of background signals represents the noise above which a ^{133}Xe signal would have to rise to garner interest.

The authors chose the 95th percentile of the distribution to be an anomaly. In other words, a signal greater than 95% of the background might trigger additional study. There are other reasons to trigger such a study—if any other explosion-related signals are seen. This might include other isotopes of xenon, aerosols, or even vibrations in the Earth, oceans, or atmosphere. In this instance, however, only the detection of one isotope is considered. The choice of 95% is not completely arbitrary, as the statistical approach of Currie (1968) chooses this level of statistical background fluctuation to set the MDC.

At this point, an action threshold can be constructed with the maximum of either the MDC or the 95th percentile. For stations that observe the analyte often, the action threshold would be the 95th percentile, and for others, any signal exceeding the MDC would garner monitoring interest. While Fig. 13 in the Appendix represented ^{133}Xe at one station for one year, the situation is quite different for

Table 3

Influence of ^{212}Pb concentrations on the MDCs for ^{140}Ba and ^{131}I for samples with detections of ^{131}I at RN70 (Sacramento, California, USA)

Collection stop	^{212}Pb conc. (µBq/m^3)	^{140}Ba MDC (µBq/m^3)	^{131}I MDC (µBq/m^3)	^{131}I conc. (µBq/m^3)
2/19/2021	45,800	14.5	5.2	3.06
5/19/2018	52,300	15.0	5.27	3.07
11/18/2017	49,300	15.5	5.34	3.73
7/9/2020	59,000	15.2	5.52	5.23
7/10/2020	79,500	16.7	6.08	4.84
7/28/2018	106,900	18.5	6.52	3.95
2/6/2016	103,400	19.8	7.06	7.36
11/20/2015	212,300	24.4	8.8	9.1
10/24/2015	238,800	24.8	9.08	23.1

Table 4

The number of ^{131}I detections and the average and 95th percentile of the ^{131}I concentrations of the detections for all IMS stations with 10 or more detections from January 2012 through February 2021

Station	MDC[a] (μBq/m^3)	Detecting samples	Average (μBq/m^3)	95th percentile (μBq/m^3)
RN61	2.34	449	9.12	29.85
RN22	5.19	224	10.2	23.35
RN21	5.42	23	11.1	20.21
RN20	4.81	145	6.36	16.92
RN01	3.78	80	4.97	14.92
RN58	4.11	14	3.43	8.07
RN52	1.98	79	2.22	4.21
RN54	2.00	76	1.93	4.18
RN50	1.54	41	1.76	3.68
RN59	3.12	12	1.49	2.99

[a]Average MDC of existing equipment. See Appendix 1 for more details

^{131}I. The frequency of historical ^{131}I detections in the entire IMS in the years 2012 through 2020 are shown in Fig. 5 as a function of concentration. About half of the detections have concentrations above 3.52 μBq/m^3 which is not too different from the MDC for that isotope. These 1234 detections occurred in 194,162 total samples.

Significant levels of ^{212}Pb are present in many of the samples with ^{131}I detections and cause substantial variation in the daily ^{131}I MDC. The concentration levels for ^{212}Pb in Table 3 are illustrated for the 9 samples with detected ^{131}I collected at RN70 (Sacramento, California, USA) and the ^{131}I MDC varies from 5 to 9 μBq/m^3. Over half of the samples contain reviewer-confirmed ^{131}I concentrations found below the calculated MDC for that sample. Only one sample is substantially above the MDC for the relevant day at the station.

There were one or more ^{131}I detections at 45 IMS aerosol stations during 2012–2020. The average and 95th percentile of ^{131}I concentrations at the IMS stations with 10 or more detections are shown in Table 4. Below this number, the 95th percentile becomes difficult to accurately estimate and is quite similar to the MDC. In Table 4, the 95th percentile ranges from about 13 times the MDC to about the same as the MDC. For half the entries in Table 4, the MDC is at most doubled by the ^{131}I background. Thus, only 5 IMS aerosol stations have a particularly significant background effect for ^{131}I. The number of ^{131}I detections for all IMS stations is provided in Appendix 1.

2.4. Atmospheric Transport Model

All atmospheric transport results in this paper used the Hybrid Single-Particle Lagrangian Integrated Trajectory (HYSPLIT) model (Stein et al., 2015), which incorporates both advective and diffusive processes. The transport runs were performed using the Linux version of HYSPLIT. Default model parameters (Draxler et al., 2020) were used. For example, vertical turbulence was simulated using the Clayson and Kantha (2008) model and horizontal turbulence is proportional to the vertical turbulence. The boundary layer stability was computed from heat and momentum fluxes read from the meteorological data files. The top of the atmospheric model domain was set to 10,000 m above ground level.

Wet and dry deposition mechanisms were deactivated for the xenon transport runs because xenon is a noble gas and its concentration in the air does not depend on rainout or deposition processes. Wet and dry deposition were included for both ^{140}Ba and ^{131}I using the assumption the transport was in particulate form. Iodine can transport as inorganic, elemental, and particulate species, and can change forms during transport. In addition, the speciation depends on the local humidity (Fitzgerald, 1975; Winkler, 1973). Modeling the different iodine species is difficult, and while it is necessary when dealing with concentrations high enough to impact human health (Eslinger et al., 2014b), this work only used the particulate iodine form. This assumption may underestimate the detection probabilities for ^{131}I.

The transport runs used to determine network performance used archived meteorological data for 2019 on a 1° spacing and 3-h time step (GDAS1, 2020). Each run modeled plume movement for 10 days and saved concentration data on a global 0.5° grid. One of the techniques developed to reduce the computational burden in a source-term analysis with far fewer samplers than possible release points is to use atmospheric transport runs done backwards in time (Hourdin & Talagrand, 2006; Hourdin et al.,

2006; Rao, 2007; Seibert & Frank, 2004; Stohl et al., 2002). Although time-reversed runs don't exactly match with forward-time runs (Eslinger & Schrom, 2019), these runs were performed in the reversed-time direction for computational convenience.

All releases from hypothetical nuclear explosions are assumed to be 3 h in length and the releases are transported through the atmosphere for 10 days after the release. This work models 8 releases per day for an entire year at a large number (258,839) of unequally spaced locations. The locations were selected on a global grid with constant 0.5° spacing in latitude and longitude. Thus, the detection statistics are based on 7.55×10^8 possible releases.

2.5. Network Performance Model

As mentioned above, the detection design goal for the IMS radionuclide (aerosol) network performance was to achieve a 90% probability of detecting an atmospheric test of 1 kiloton TNT equivalent explosion within 10 days (IMS Expert Group, 1995; Werzi, 2009). In this work, a network detection metric is used to assess the probability of detection for a release at an unknown time and unknown location. As noted by Kalinowski (2001) and others, radionuclide samples and atmospheric transport modeling can be used for several purposes in addition to just detecting a release, such as locating the release point. Thus, we define three network metrics. The first metric is the probability a release is detected. The second and third metrics are the expected number of detecting samples and the expected number of detecting stations. In general, obtaining more samples with detections at more stations helps in determining the timing and location of the release event.

Consider the situation where there are N_s radioisotope samplers at different locations around the globe. In an abstract sense, each sampler has a probability of detecting a specific future release of a radioactive isotope. This detection probability depends on the location of the release, the magnitude of the release, the specific radioisotope, the sampling duration, the detection sensitivity of the equipment, and future atmospheric circulation patterns. One way to compare system performance for different network configurations is to define a detection metric for the entire global network. The same type of metric can be applied for smaller regions.

Suppose that the surface area of the globe is partitioned into a large number, N_r, of regions, each with surface area A_i, for $i = 1,\ldots, N_r$. In general, the surface area of the regions may not be equal. Then, denote the probability, $P(M,R_s)$, that a radioisotope release of a given magnitude, M, occurring in a specific region R_s at a series of times t_j, for $j = 1, \ldots, N_t$ is detected by one or more samplers. This can be expressed in the following mathematical form:

$$P(M,R_s) = \frac{1}{N_t}\sum_{j=1}^{N_t} I(\textit{One or more samplers detected release } j \textit{ from} R_s) \quad (2)$$

where I(·) is the indicator function, which takes the value 1 when true and 0 when false. The network detection metric, $D(M)$, defined for a release of magnitude M, given a network of N_k sampling locations, and a surface area partitioned into N_r regions, is:

$$D(M) = \frac{\sum_{i=1}^{N_r} A_i \times P(M,R_i)}{\sum_{i=1}^{N_r} A_i} \quad (3)$$

Below, we use the notation $D(15)_{39}$ to denote a release magnitude of 10^{15} Bq and a network size of 39 stations. If the surface areas of the regions are all of the same size, such as used by Schoeppner and Plastino (2014), then Eq. 3 simplifies to an average value:

$$D(M) = \frac{1}{N_r}\sum_{i=1}^{N_r} P(M,R_i) \quad (4)$$

The network metric satisfies $0 \le D(M) \le 1$. A value of 0 indicates that a release of magnitude M will not be detected by any sampling station, no matter when or where the release occurs. A value of 1 indicates that a release of magnitude M will always be detected by at least one sampling station, no matter when or where the release occurs.

Determination of the release location from radionuclide samples becomes more important for small underground nuclear explosions than for large atmospheric nuclear explosive tests. Seismologists need a minimum of three sampling stations to

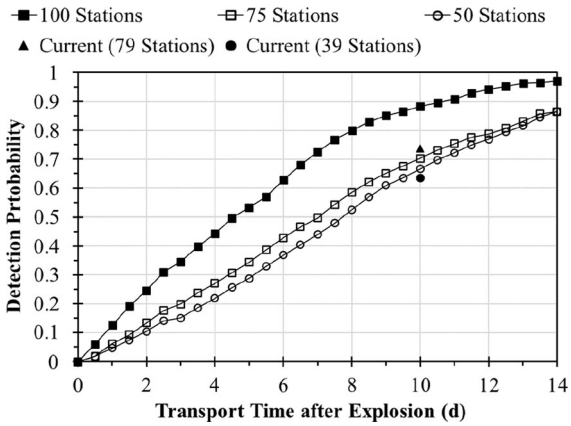

Figure 6
Historical estimates of detection probabilities for different network designs, each assuming a release of 10^{15} Bq of ^{140}Ba. Our calculated performance of a 39-station network (black circle) and a 79-station network (black triangle) using 10 days of transport time past the release event and historical data for detection limits. The curves are derived from Fig. 3-1 of WP.224

pinpoint the epicenter of an earthquake. Similarly, samples at multiple locations helps in a source location analysis using airborne radionuclides. The detection metric, as formulated here, declares a detection of a release event if the concentration at one or more samples at one or more locations exceeds the detection threshold denoted by the MDC in response to that release.

We define, *N(M)*, the expected number of detecting stations over all release events as:

$$N(M) = \frac{1}{N_r \sum_{i=1}^{N_r} A_i} \sum_{i=1}^{N_r} A_i \left(\sum_{j=1}^{k} I_j(M, R_i) \right) \quad (5)$$

where $I_j(M, R_i)$ is 1 if station j detects a release of magnitude M in the region R_i in one or more samples and takes a value of 0 otherwise.

We define, *S(M)*, the expected number of detected samples over all release events as:

$$S(M) = \frac{1}{N_r \sum_{i=1}^{N_r} A_i} \sum_{i=1}^{N_r} A_i (C_i(M)) \quad (6)$$

where $C_i(M)$ counts the number of samples, across all stations, that detects release i of magnitude M.

3. Results

Network performance results for ^{140}Ba are provided in Sect. 3.1, including a comparison with performance predictions made in 1995. Section 3.2 contains network performance results for ^{131}I. Finally, network performance results for ^{133}Xe are provided in Sect. 3.3.

3.1. Network Detection Performance for ^{140}Ba

Historical estimates of the detection performance an aerosol network for ^{140}Ba for networks with 50,

Table 5
Detection performance for ^{140}Ba for different levels of release for two network sizes

Release	39 stations			79 stations		
Bq of ^{140}Ba	D(M)[a]	N(M)[b]	S(M)[c]	D(M)	N(M)	S(M)
10^{10}	0.017 ± 0.004	0.017 ± 0.004	0.020 ± 0.005	0.037 ± 0.006	0.038 ± 0.007	0.046 ± 0.009
10^{11}	0.081 ± 0.014	0.085 ± 0.018	0.127 ± 0.032	0.159 ± 0.019	0.182 ± 0.028	0.276 ± 0.048
10^{12}	0.262 ± 0.026	0.326 ± 0.048	0.606 ± 0.114	0.424 ± 0.029	0.669 ± 0.081	1.259 ± 0.175
10^{13}	0.500 ± 0.047	0.830 ± 0.121	1.743 ± 0.286	0.678 ± 0.035	1.664 ± 0.228	3.496 ± 0.525
10^{14}	0.606 ± 0.062	1.208 ± 0.193	2.671 ± 0.469	0.765 ± 0.040	2.391 ± 0.378	5.272 ± 0.897
10^{15}	0.635 ± 0.069	1.337 ± 0.222	3.009 ± 0.544	0.790 ± 0.043	2.642 ± 0.424	5.931 ± 1.041

The ± values give an approximate 95% uncertainty range for daily performance

[a]D(M) denotes the network detection probability for releases of magnitude M using Eq. (3)

[b]N(M) denotes the average number of stations that detect releases of magnitude M using Eq. (5)

[c]S(M) denotes the average number of samples that detect releases of magnitude M using Eq. (6)

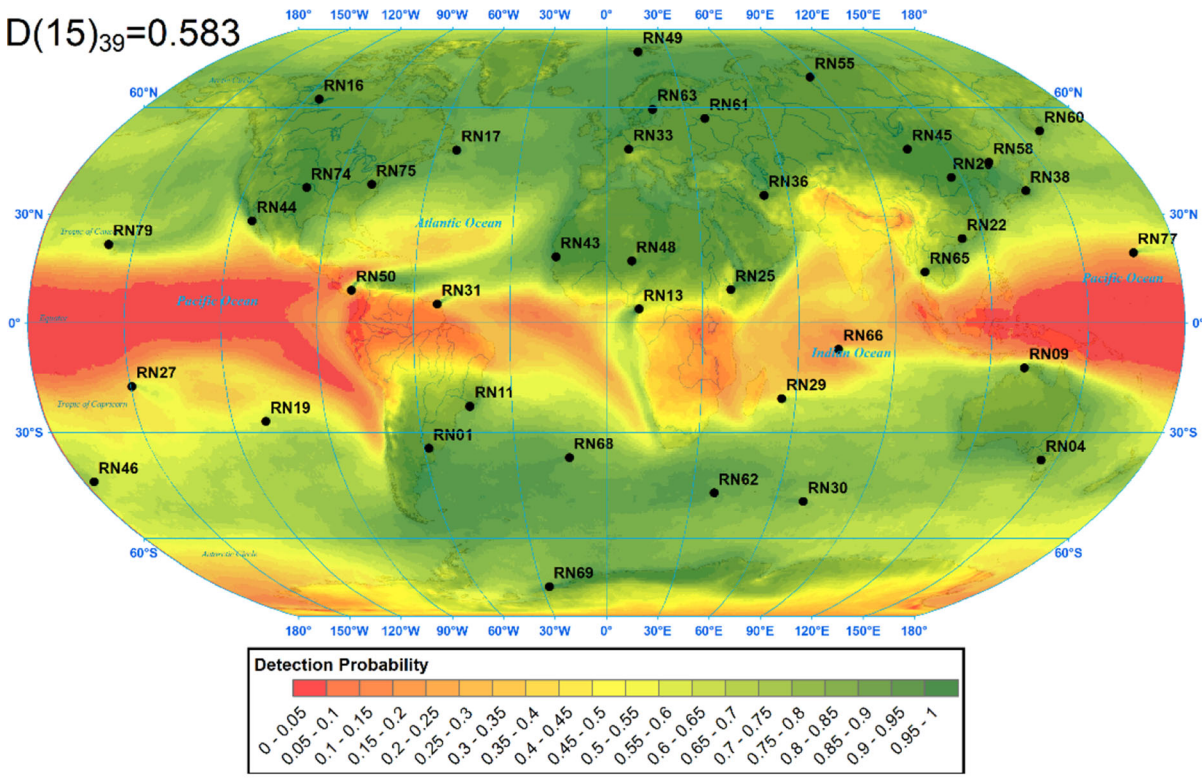
D(15)39=0.583
RN49
RN55
RN16
RN63
RN61
RN60
RN17
RN33
RN45
RN58
RN74
RN75
RN20
RN38
RN36
RN44
Atlantic Ocean
RN22
RN79
RN43
RN48
RN77
RN65
RN50
RN25
Pacific Ocean
RN31
RN13
RN66
RN09
RN27
Indian Ocean
RN11
RN29
RN19
RN01
RN68
RN04
RN46
RN62
RN30
RN69
Detection Probability
0 - 0.05
0.05 - 0.1
0.1 - 0.15
0.15 - 0.2
0.2 - 0.25
0.25 - 0.3
0.3 - 0.35
0.35 - 0.4
0.4 - 0.45
0.45 - 0.5
0.5 - 0.55
0.55 - 0.6
0.6 - 0.65
0.65 - 0.7
0.7 - 0.75
0.75 - 0.8
0.8 - 0.85
0.85 - 0.9
0.9 - 0.95
0.95 - 1

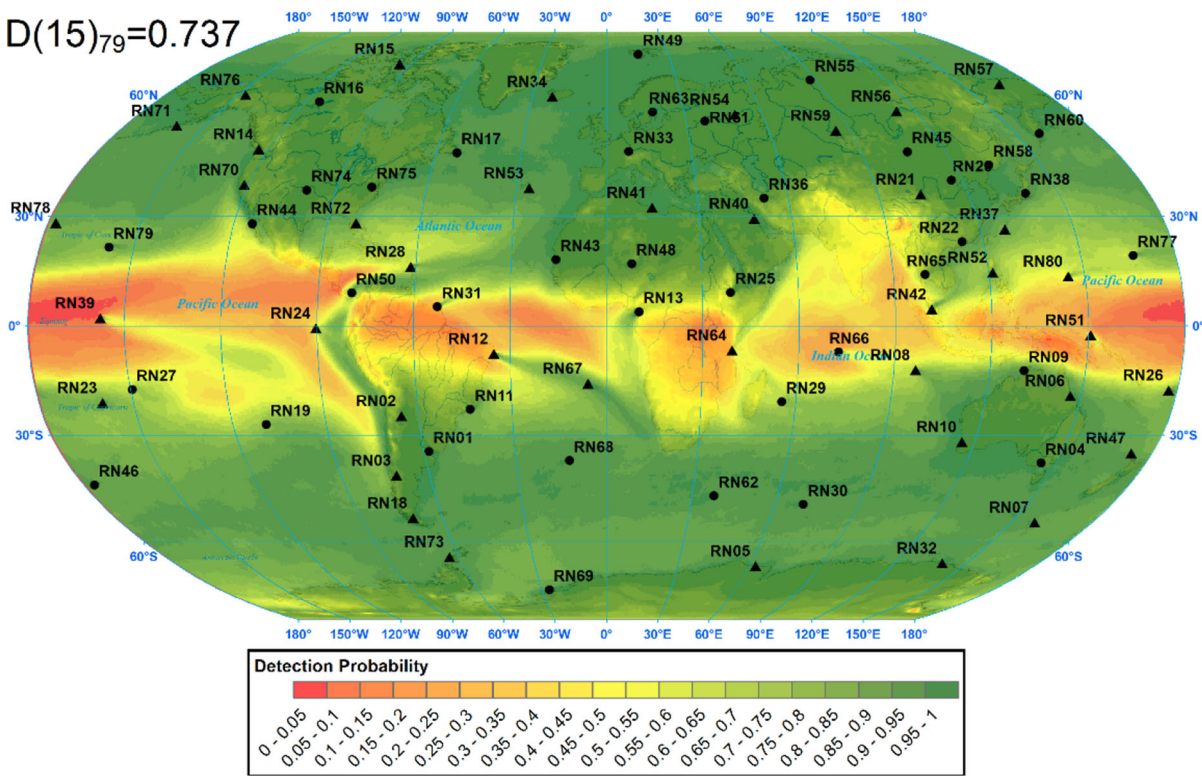
D(15)79=0.737
RN15
RN49
RN76
RN55
RN57
RN16
RN34
RN63
RN54
RN56
RN71
RN61
RN59
RN60
RN14
RN17
RN33
RN45
RN58
RN70
RN74
RN75
RN53
RN20
RN38
RN41
RN36
RN21
RN78
RN44
RN72
RN40
RN37
Atlantic Ocean
RN22
RN79
RN77
RN28
RN43
RN48
RN65
RN52
RN80
RN50
RN25
Pacific Ocean
RN39
RN31
RN42
RN24
RN13
RN51
RN12
RN64
RN66
RN67
RN08
RN09
RN23
RN27
RN29
RN06
RN26
RN02
RN11
RN19
RN10
RN01
RN47
RN68
RN04
RN03
RN46
RN62
RN30
RN18
RN07
RN73
RN05
RN32
RN69
Detection Probability
0 - 0.05
0.05 - 0.1
0.1 - 0.15
0.15 - 0.2
0.2 - 0.25
0.25 - 0.3
0.3 - 0.35
0.35 - 0.4
0.4 - 0.45
0.45 - 0.5
0.5 - 0.55
0.55 - 0.6
0.6 - 0.65
0.65 - 0.7
0.7 - 0.75
0.75 - 0.8
0.8 - 0.85
0.85 - 0.9
0.9 - 0.95
0.95 - 1

◀Figure 7
Network detection probabilities for 39-station (upper panel) and 79-station (lower panel) networks assuming a release of 10^{15} Bq of ^{140}Ba anywhere on the globe. Detection limits for each station were derived from historical measurements. This activity level roughly corresponds to 100 tons of fission yield

75, and 100 stations for a range of transport times are shown in Fig. 6 for a design basis release of 10^{15} Bq of ^{140}Ba to the atmosphere and an MDC of 10 μBq/m^3. Figure 6 is derived from Fig. 3-1 of WP.224 (IMS Expert Group, 1995). The detection probability, D(M), calculated using Eq. (3), is shown for a 39-station network (black circle) and a 79-station network (black triangle) event and historical data for detection limits. The current performance estimate for ^{140}Ba matches nicely with the historical estimates of the design-basis performance.

The performance of 39- and 79-station networks for the detection of ^{140}Ba are shown in Table 5 for a large range of release magnitudes. The 39-station network uses the 39 stations with existing or planned noble gas systems (CTBTO PrepCom, 2020). The historical average ^{140}Ba MDC was used for 72 of the stations. The stations without operating systems were assigned the MDCs from other stations currently operating on the same continent. Details of the assignments of the MDCs are provided in Appendix 1. The performance statistics in Table 5 are averaged over a year for the entire globe. The same statistics can be evaluated for shorter time periods, such as a day, to give an idea of the temporal variation in detection capabilities. The ± values represent an approximate 95% uncertainty range on daily D(M), N(M), and S(M) values.

The network coverage varies in space as well as in time. The network detection probabilities for 39-station and 79-station networks are shown in Fig. 7, assuming a release of 10^{15} Bq of ^{140}Ba anywhere on the globe. Detection limits for each station were derived from historical measurements as described in Appendix 1. The average number of stations that would detect a release of 10^{15} Bq of ^{140}Ba anywhere on the globe for 39- and 79-station networks are provided in Fig. 8. This result was expected when the IMS system was designed (IMS Expert Group, 1995) but can now be evaluated through extensive transport simulations.

The overall network performance of the 79-station IMS RN network for a release of 10^{15} Bq of ^{140}Ba is remarkably close to the historical estimate. Even with the unexpected (in 1995) impact of ^{212}Pb on the ^{140}Ba detection limit, the average MDC across 79 stations is 9.92 μBq/m^3, while the design basis was 10 μBq/m^3. As shown in Figs. 7 and 8, coverage in the equatorial regions is poorer than at higher latitudes. This result was expected when the system was designed (IMS Expert Group, 1995) but can now be evaluated through extensive transport simulations. Increasing the number of noble gas stations from 39 to 79, as is allowed in the treaty after entry into force, improves D(M), but it nearly doubles N(M) and S(M). Having more detecting stations and samples is important for improving the accuracy of the estimated release location from the sampling data, as shown in Eslinger and Schrom (2016). The maps of the number of detecting stations calculated for this analysis are similar to those produced by (Werzi, 2009) for a few months.

3.2. *Network Detection Performance for ^{131}I*

The performance of 39- and 79-station networks for the detection of ^{131}I are shown in Table 6. The 39-station network uses the 39 stations with existing or planned noble gas systems (CTBTO PrepCom, 2020). The historical average ^{131}I MDC was used for 72 of the stations. The stations without operating systems were assigned the MDCs from other stations currently operating on the same continent. Details of the assignments of the MDCs are provided in Appendix 1. The performance statistics in Table 6 are averaged over a year for the entire globe. The ± values represent an approximate 95% uncertainty range on daily D(M), N(M), and S(M) values.

The network detection probabilities for a 79-station network are shown in Fig. 9, assuming a release of 10^{11} Bq of ^{131}I anywhere on the globe. Detection limits for each station were derived from historical measurements as described in Appendix 1. The decrease in the detection probability when the station detection limits are raised to the 95th percentile of

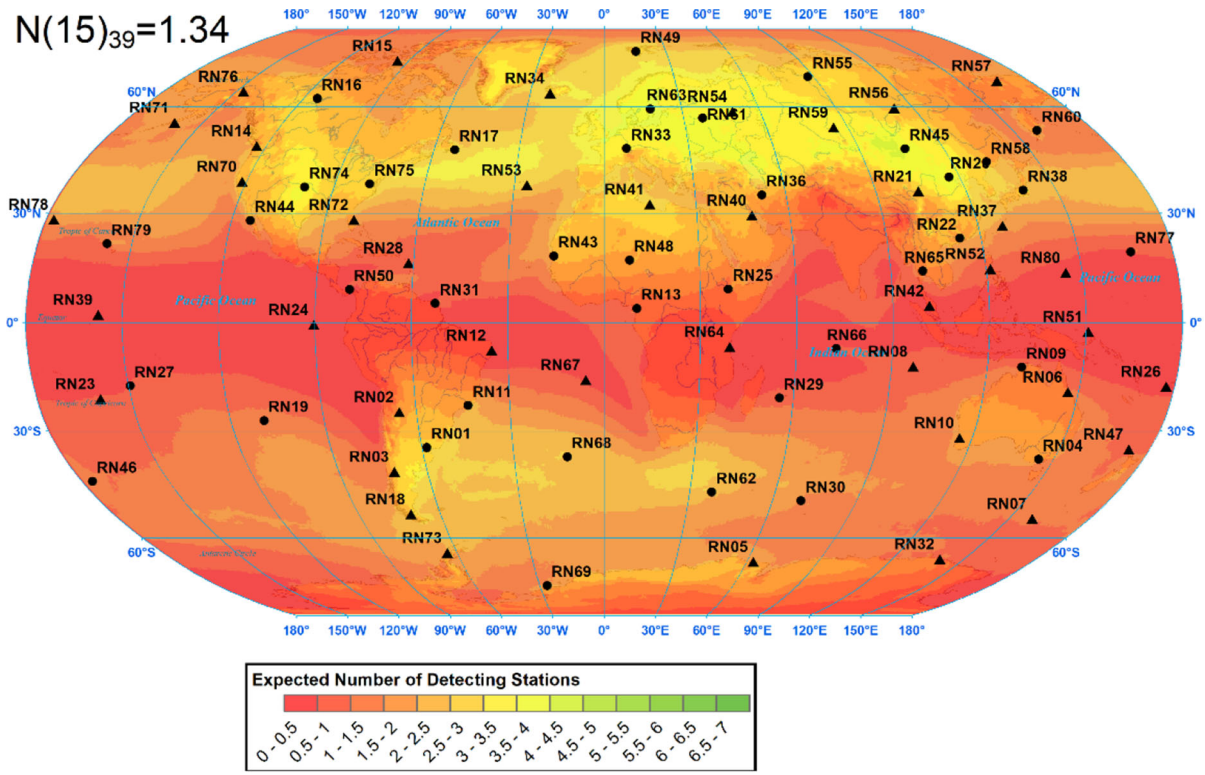
N(15)39=1.34
RN15
RN49
RN76
RN16
RN34
RN55
RN57
RN71
RN63
RN54
RN61
RN56
RN60
RN14
RN17
RN33
RN59
RN45
RN58
RN70
RN74
RN75
RN53
RN41
RN36
RN21
RN20
RN38
RN78
RN44
RN72
RN40
RN37
RN79
RN22
RN77
RN28
RN43
RN48
RN65
RN52
RN80
RN50
RN25
RN39
RN31
RN13
RN42
RN24
RN51
RN12
RN64
RN66
RN08
RN09
RN67
RN06
RN26
RN23
RN27
RN29
RN02
RN11
RN19
RN10
RN47
RN01
RN68
RN04
RN03
RN46
RN62
RN30
RN18
RN07
RN73
RN05
RN32
RN69
Expected Number of Detecting Stations
0 - 0.5
0.5 - 1
1 - 1.5
1.5 - 2
2 - 2.5
2.5 - 3
3 - 3.5
3.5 - 4
4 - 4.5
4.5 - 5
5 - 5.5
5.5 - 6
6 - 6.5
6.5 - 7

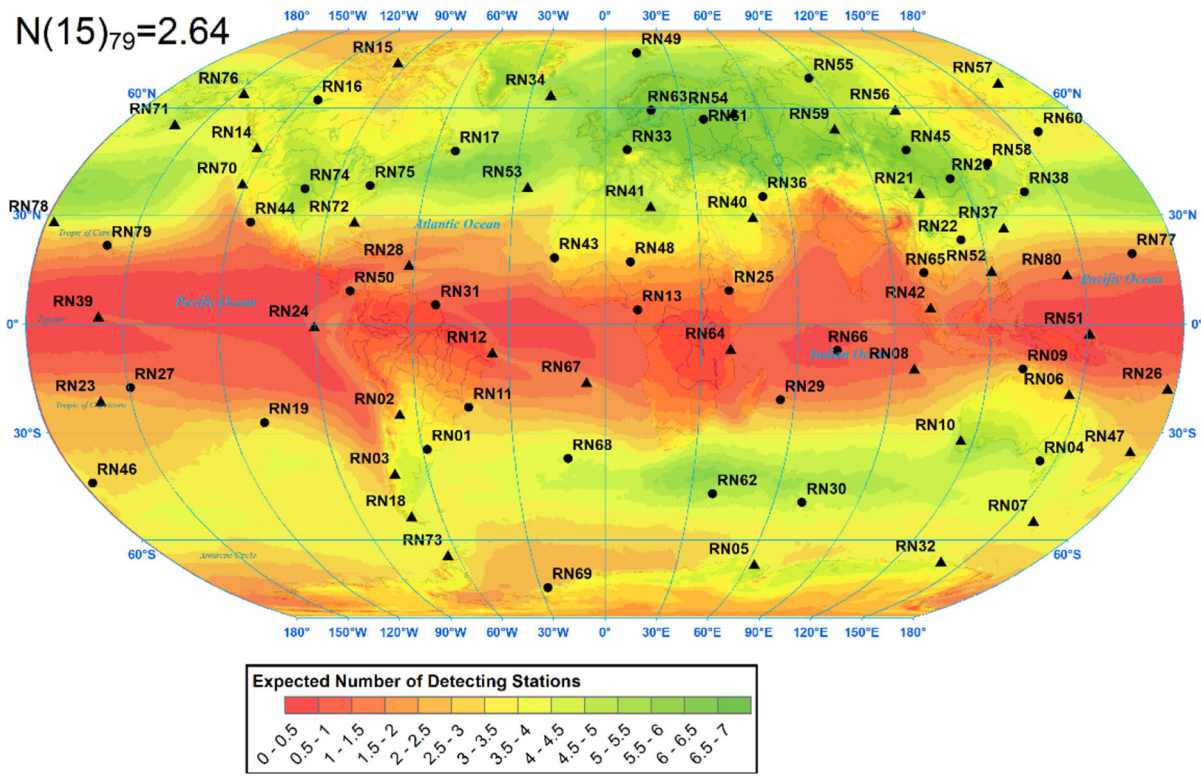
N(15)79=2.64
RN15
RN49
RN76
RN16
RN34
RN55
RN57
RN71
RN63
RN54
RN61
RN56
RN60
RN14
RN17
RN33
RN59
RN45
RN58
RN70
RN74
RN75
RN53
RN41
RN36
RN21
RN20
RN38
RN78
RN44
RN72
RN40
RN37
RN79
RN22
RN77
RN28
RN43
RN48
RN65
RN52
RN80
RN50
RN25
RN39
RN31
RN13
RN42
RN24
RN51
RN12
RN64
RN66
RN08
RN09
RN67
RN06
RN26
RN23
RN27
RN29
RN02
RN11
RN19
RN10
RN47
RN01
RN68
RN04
RN03
RN46
RN62
RN30
RN18
RN07
RN73
RN05
RN32
RN69
Expected Number of Detecting Stations
0 - 0.5
0.5 - 1
1 - 1.5
1.5 - 2
2 - 2.5
2.5 - 3
3 - 3.5
3.5 - 4
4 - 4.5
4.5 - 5
5 - 5.5
5.5 - 6
6 - 6.5
6.5 - 7

◀Figure 8
Average number of stations that would detect a release of 10^{15} Bq of ^{140}Ba anywhere on the globe for 39-station (upper panel) and 79-station (lower panel) networks. Detection limits for each station were derived from historical measurements

historical detections at the station is also shown in Fig. 9.

The network-level results in Table 6 and the spatial coverage in Fig. 9 show that the coverage of the IMS radionuclide network is poor for a nominal release of 10^{11} Bq of ^{131}I, especially in the equatorial regions. As shown in Table 6, the percent decreases in detection probabilities due to background sources of ^{131}I are nonnegligible, but they are more pronounced for a 39-station network than for a 79-station network. Also, next generation aerosol samplers currently under development (Miley et al., 2019) may have lower MDCs and shorter sampling periods. These changes would improve the detection capabilities, including providing more samples with concentrations above the detection limits.

Medical isotope production facilities that release some ^{131}I to the atmosphere are located in Argentina (South America), in China, and in the Russian Federation. The fourth region with elevated background levels of ^{131}I is in Panama, Central America. There is no known medical isotope production near this station, but exhalation of ^{131}I by multiple patients treated with ^{131}I for medical procedures (Gründel et al., 2008) near the sampler might release enough ^{131}I to result in occasional detections (Miley et al., 2021).

3.3. Network Detection Performance for ^{133}Xe

As of the start of 2021, only 25 locations had xenon systems certified for operation in the IMS, and these fall into three system types (Dubasov et al., 2005; Fontaine et al., 2004; Ringbom et al., 2003) with different performance characteristics. Many of the certified systems have processed thousands of samples over several years and thus have a well-established background history, such as that in Fig. 13 of the Appendix. This history indicates that presence of the analyte of interest, ^{133}Xe, is the dominant monitoring challenge for many locations.

The network performance estimates for ^{133}Xe use modeled concentrations from nuclear power plants and medical isotope production facilities to determine the 95th percentile anomaly level. As shown in

Table 6

Detection performance for ^{131}I for different levels of release for two network sizes

Number stations	Release (Bq)	D(M)[a]	N(M)[b]	S(M)[c]	ΔD(M)[d] %	ΔN(M) %	ΔS(M) %
39	10^{10}	0.034 ± 0.007	0.034 ± 0.008	0.044 ± 0.011	11.3	11.7	12.2
39	10^{11}	0.135 ± 0.020	0.149 ± 0.028	0.243 ± 0.056	8.2	10.0	11.0
39	10^{12}	0.358 ± 0.033	0.494 ± 0.067	0.974 ± 0.161	5.2	9.0	10.0
39	10^{13}	0.555 ± 0.053	1.002 ± 0.149	2.161 ± 0.360	2.4	6.0	6.6
39	10^{14}	0.620 ± 0.065	1.270 ± 0.206	2.835 ± 0.502	0.7	2.2	2.6
39	10^{15}	0.640 ± 0.070	1.358 ± 0.227	3.068 ± 0.554	0.3	0.7	0.9
79	10^{10}	0.072 ± 0.011	0.076 ± 0.013	0.099 ± 0.018	6.3	6.9	7.3
79	10^{11}	0.250 ± 0.024	0.313 ± 0.043	0.519 ± 0.081	4.4	6.2	6.8
79	10^{12}	0.539 ± 0.031	1.007 ± 0.121	2.001 ± 0.265	2.3	5.8	6.4
79	10^{13}	0.725 ± 0.036	1.999 ± 0.289	4.305 ± 0.673	0.9	4.0	4.4
79	10^{14}	0.777 ± 0.041	2.513 ± 0.397	5.594 ± 0.964	0.3	1.5	1.8
79	10^{15}	0.795 ± 0.044	2.686 ± 0.431	6.048 ± 1.065	0.1	0.5	0.6

The ± values give an approximate 95% uncertainty range for daily performance

[a]D(M) denotes the network detection probability for releases of magnitude M using Eq. (3)

[b]N(M) denotes the average number of stations that detect releases of magnitude M using Eq. (5)

[c]S(M) denotes the average number of samples that detect releases of magnitude M using Eq. (6)

[d]The Δ notation is the decrease in coverage when the station MDCs are adjusted to the 95th percentile of background samples. For example, an 11.3% decrease in D(M) for a 10^{10} Bq release and a 39-station network lowers the D(M) value from 0.034 to 0.030

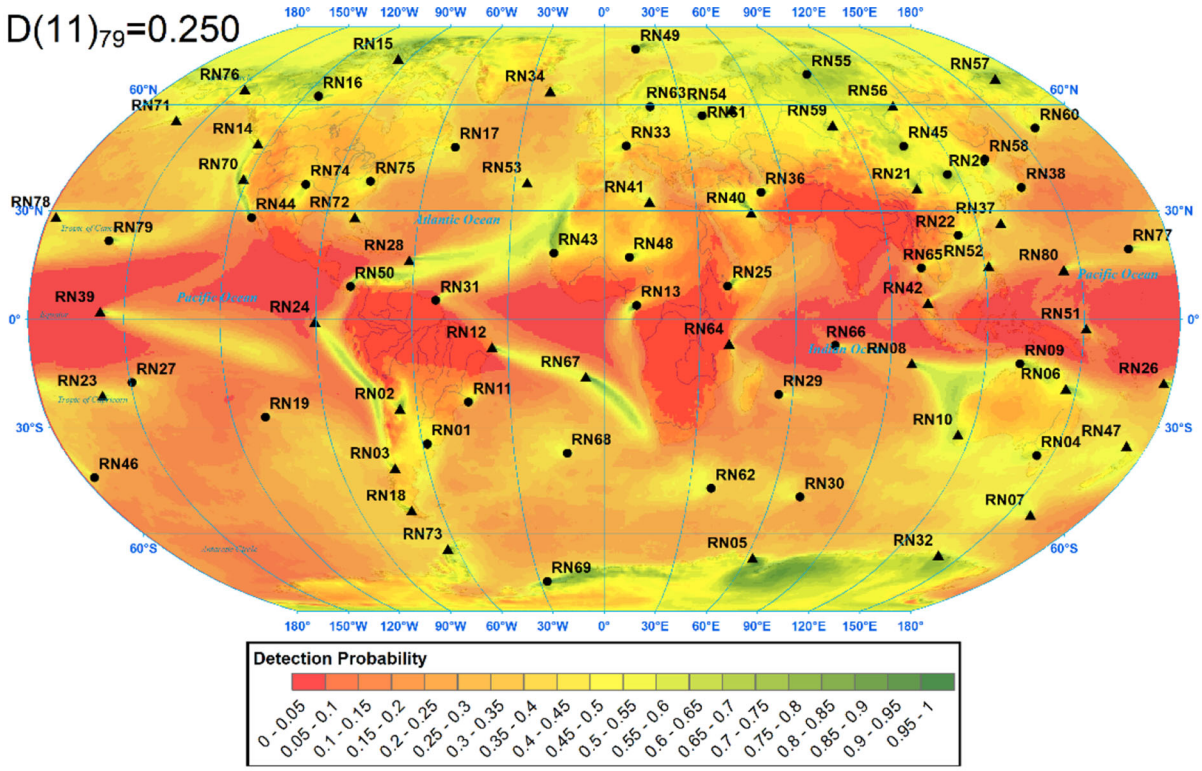
D(11)79=0.250
RN15
RN49
RN76
RN16
RN34
RN55
RN57
RN63
RN54
RN56
RN71
RN61
RN59
RN60
RN14
RN17
RN33
RN45
RN58
RN70
RN74
RN75
RN53
RN20
RN38
RN78
RN44
RN72
RN41
RN36
RN21
RN37
RN79
RN22
RN77
RN28
RN43
RN48
RN65
RN52
RN80
RN50
RN25
RN39
RN31
RN13
RN42
RN24
RN51
RN12
RN64
RN66
RN08
RN09
RN67
RN06
RN26
RN23
RN27
RN29
RN19
RN02
RN11
RN10
RN01
RN04
RN47
RN68
RN46
RN03
RN62
RN30
RN18
RN07
RN73
RN05
RN32
RN69
Detection Probability
0 - 0.05
0.05 - 0.1
0.1 - 0.15
0.15 - 0.2
0.2 - 0.25
0.25 - 0.3
0.3 - 0.35
0.35 - 0.4
0.4 - 0.45
0.45 - 0.5
0.5 - 0.55
0.55 - 0.6
0.6 - 0.65
0.65 - 0.7
0.7 - 0.75
0.75 - 0.8
0.8 - 0.85
0.85 - 0.9
0.9 - 0.95
0.95 - 1

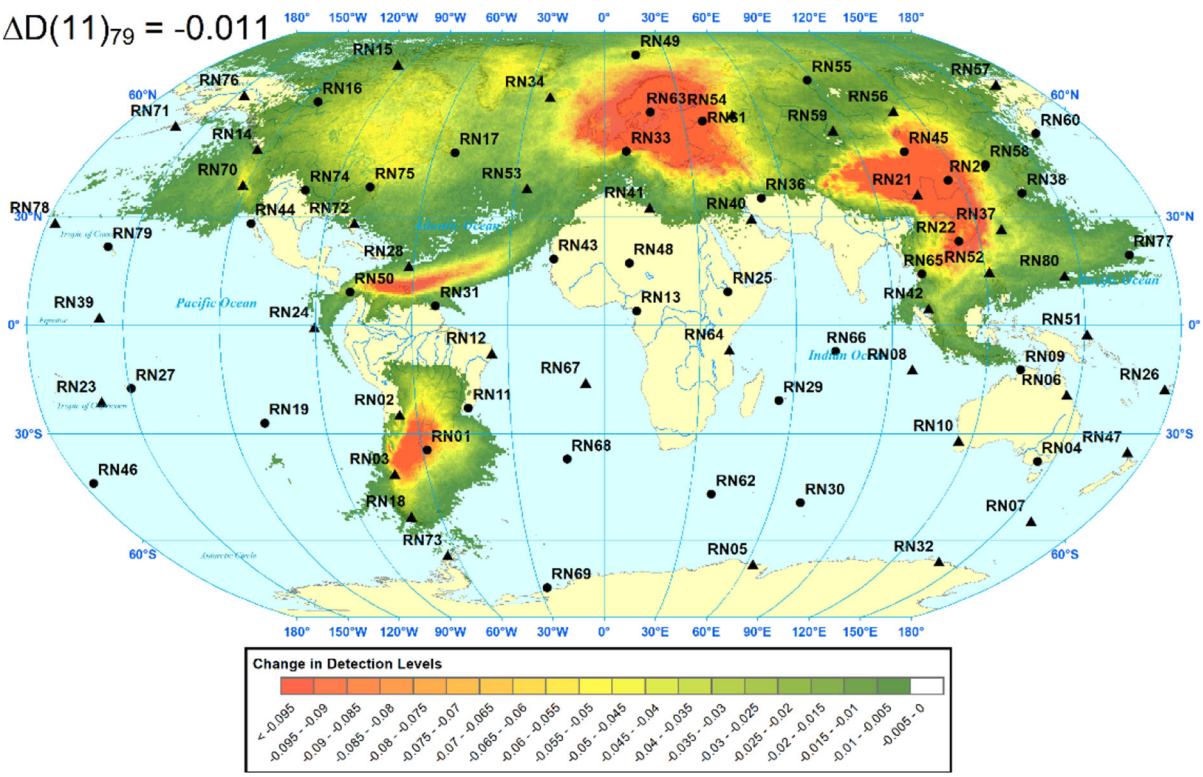
ΔD(11)79 = -0.011
RN15
RN49
RN76
RN16
RN34
RN55
RN57
RN63
RN54
RN56
RN71
RN61
RN59
RN60
RN14
RN17
RN33
RN45
RN58
RN70
RN74
RN75
RN53
RN20
RN38
RN78
RN44
RN72
RN41
RN36
RN21
RN37
RN79
RN22
RN77
RN28
RN43
RN48
RN65
RN52
RN80
RN50
RN25
RN39
RN31
RN13
RN42
RN24
RN51
RN12
RN64
RN66
RN08
RN09
RN67
RN06
RN26
RN23
RN27
RN29
RN19
RN02
RN11
RN10
RN01
RN04
RN47
RN68
RN46
RN03
RN62
RN30
RN18
RN07
RN73
RN05
RN32
RN69
Change in Detection Levels
< -0.095
-0.095 - -0.09
-0.09 - -0.085
-0.085 - -0.08
-0.08 - -0.075
-0.075 - -0.07
-0.07 - -0.065
-0.065 - -0.06
-0.06 - -0.055
-0.055 - -0.05
-0.05 - -0.045
-0.045 - -0.04
-0.04 - -0.035
-0.035 - -0.03
-0.03 - -0.025
-0.025 - -0.02
-0.02 - -0.015
-0.015 - -0.01
-0.01 - -0.005
-0.005 - 0

◀Figure 9
Detection probabilities for a 79-station network for a 10^{11} Bq of ^{131}I anywhere on the globe (upper panel). The decrease in the detection probability when the station detection limits are raised to an anomaly level equal to the 95th percentile of historical detections at that station is shown in the lower pane. For example, the coverage in a region with a bright red contour has an absolute decrease in D(M) of around 0.1, which could correspond to as much as a 40% decrease in the detections in that local region

Appendix 1, the 95th percentile of modeled ^{133}Xe concentrations can be close to the measured values for some stations. The results are similar to that of Achim et al. (2016) and Schoeppner and Plastino (2014). In addition, Gueibe et al. (2017) compared modeled and measured concentrations in the IMS for four xenon isotopes. An action threshold is then created using the maximum of either the MDC for the system presumed to operate at that station or the 95th percentile of the estimated background.

The performance of 39- and 79-station networks for the detection of ^{133}Xe are shown in Table 7. Published MDCs are used for currently deployed sampling equipment. Details of the assignments of the MDCs are provided in Appendix 1. The columns in Table 7 with a Δ in the header show the percent decrease in performance when the MDC is set to the maximum of the equipment level and the 95th percentile of the modeled background concentrations. The performance statistics in Table 7 are averaged over a year for the entire globe. The ± values represent an approximate 95% uncertainty range on daily D(M), N(M), and S(M) values. Increasing the MDC to an anomaly threshold based on the background levels causes significant reductions in detection performance, especially for lower release magnitudes. Adding additional sampling locations improves the overall performance but does not mitigate effects of background ^{133}Xe.

The estimated performance of a 100-station network given in Fig. 3-3 of WP.224 was about 0.2 for a release of 10^{15} Bq, assuming a detection limit of 1 mBq/m^3. Our calculations of the detection probability for the smaller 39-station network for a release of 10^{15} Bq is 0.7, much better than the historical performance estimate. We calculated a D(M) of 0.9 for a 100-station network formed by adding another 21 stations to the existing radionuclide stations while assuming a 10^{15} Bq release of ^{133}Xe and an MDC of 1.0 mBq/m^3 for every sampler.

Table 7

Detection performance for ^{133}Xe for different levels of release for two network sizes

Number stations	Release (Bq)	D(M)[a]	N(M)[b]	S(M)[c]	ΔD(M)[d] %	ΔN(M) %	ΔS(M) %
39	10^{10}	0.0016 ± 0.0003	0.0016 ± 0.0003	0.0019 ± 0.0004	27.6	27.6	29.1
39	10^{11}	0.013 ± 0.002	0.013 ± 0.002	0.017 ± 0.003	27.5	27.6	29.4
39	10^{12}	0.070 ± 0.011	0.072 ± 0.011	0.120 ± 0.020	29.4	30.1	32.8
39	10^{13}	0.270 ± 0.036	0.317 ± 0.043	0.752 ± 0.127	27.6	32.5	34.9
39	10^{14}	0.591 ± 0.066	1.077 ± 0.137	3.286 ± 0.448	16.3	32.7	34.1
39	10^{15}	0.703 ± 0.080	1.768 ± 0.266	6.052 ± 0.947	5.2	22.6	24.4
79	10^{10}	0.003 ± 0.001	0.003 ± 0.001	0.004 ± 0.001	23.9	23.9	24.8
79	10^{11}	0.026 ± 0.004	0.026 ± 0.004	0.034 ± 0.006	23.0	23.0	24.2
79	10^{12}	0.135 ± 0.017	0.142 ± 0.019	0.235 ± 0.037	23.7	24.7	26.8
79	10^{13}	0.449 ± 0.042	0.618 ± 0.077	1.455 ± 0.222	18.7	26.0	28.3
79	10^{14}	0.765 ± 0.046	2.093 ± 0.256	6.384 ± 0.838	7.2	26.3	27.8
79	10^{15}	0.839 ± 0.048	3.468 ± 0.495	11.877 ± 1.765	1.7	17.9	19.7

The ± values give an approximate 95% uncertainty range for daily performance

[a]D(M) denotes the network detection probability for releases of magnitude M using Eq. (3)

[b]N(M) denotes the average number of stations that detect releases of magnitude M using Eq. (5)

[c]S(M) denotes the average number of samples that detect releases of magnitude M using Eq. (6)

[d]The Δ notation is the decrease in coverage when the station MDCs are adjusted up to the 95th percentile of modeled background

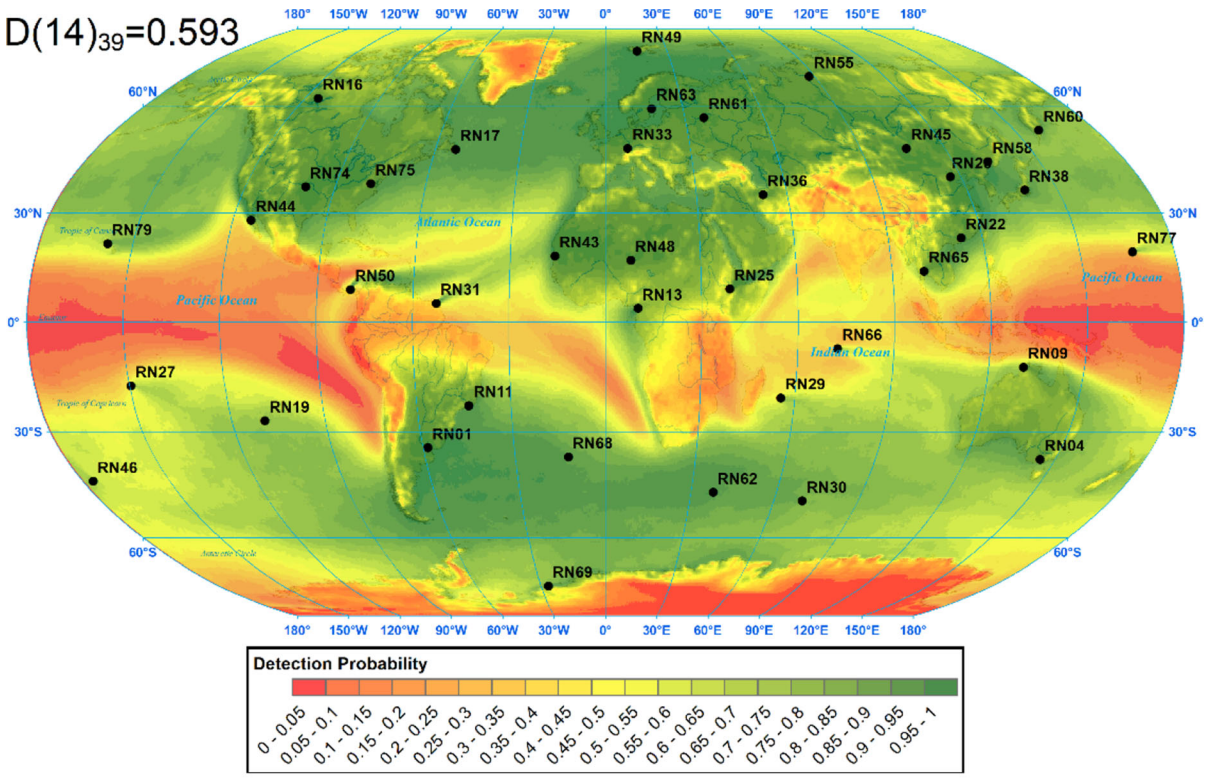
D(14)39=0.593
RN49
RN55
RN16
RN63
RN61
RN60
RN17
RN33
RN45
RN58
RN74
RN75
RN20
RN38
RN36
RN44
RN22
RN79
RN43
RN48
RN77
RN65
RN50
RN31
RN25
RN13
RN66
RN09
RN27
RN11
RN29
RN19
RN01
RN68
RN04
RN46
RN62
RN30
RN69
Detection Probability
0 - 0.05
0.05 - 0.1
0.1 - 0.15
0.15 - 0.2
0.2 - 0.25
0.25 - 0.3
0.3 - 0.35
0.35 - 0.4
0.4 - 0.45
0.45 - 0.5
0.5 - 0.55
0.55 - 0.6
0.6 - 0.65
0.65 - 0.7
0.7 - 0.75
0.75 - 0.8
0.8 - 0.85
0.85 - 0.9
0.9 - 0.95
0.95 - 1

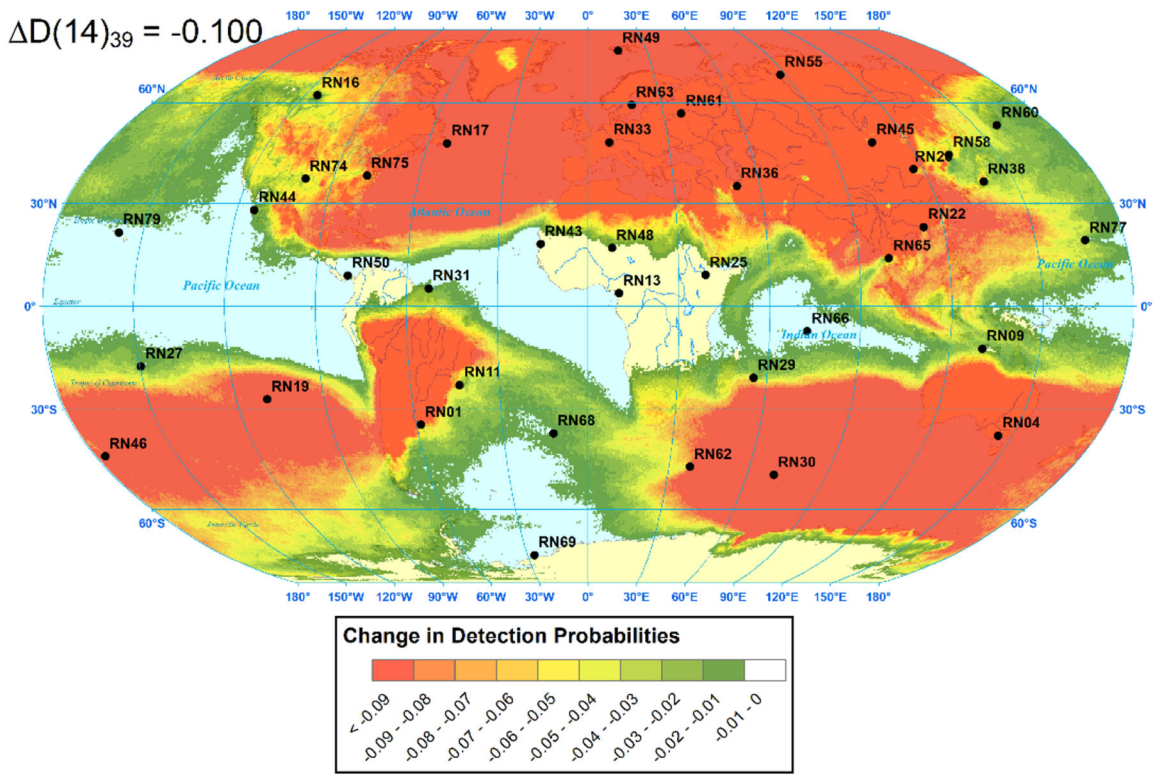
ΔD(14)39 = -0.100
RN49
RN55
RN16
RN63
RN61
RN60
RN17
RN33
RN45
RN58
RN74
RN75
RN20
RN38
RN36
RN44
RN22
RN79
RN43
RN48
RN77
RN65
RN50
RN31
RN25
RN13
RN66
RN09
RN27
RN11
RN29
RN19
RN01
RN68
RN04
RN46
RN62
RN30
RN69
Change in Detection Probabilities
< -0.09
-0.09 - -0.08
-0.08 - -0.07
-0.07 - -0.06
-0.06 - -0.05
-0.05 - -0.04
-0.04 - -0.03
-0.03 - -0.02
-0.02 - -0.01
-0.01 - 0

◀Figure 10
Detection probabilities for a 39-station network for a 10^{14} Bq release of ^{133}Xe anywhere on the globe (upper pane). Change in the detection probability when the station detection limits are raised to an anomaly level equal to the 95th percentile of modeled background (lower pane)

The network detection probabilities for a 39-station network are shown in Fig. 10, assuming a release of 10^{14} Bq of ^{133}Xe anywhere on the globe. The 10^{14} Bq release level was chosen mostly because two of the tests conducted by the DPRK (Murphy et al., 2013; Ringbom et al., 2009, 2014) may have had releases on the order of 10^{14} Bq of ^{133}Xe.

Detection limits for each station were derived from equipment specifications and modeled backgrounds from nuclear power plants and medical isotope production facilities as described in Appendix 1. The decrease in the detection probability when the station detection limits are raised to the 95th percentile of modeled backgrounds is also shown in Fig. 10. Using the same assumptions, the network detection probabilities for a 79-station network are shown in Fig. 11.

The network-level results in Table 7 and the spatial coverage in Fig. 10 show that the coverage of the IMS radionuclide network is poor for a nominal release of 10^{14} Bq of ^{133}Xe, especially in the equatorial regions. Following entry into force of the treaty, the addition of more IMS RN station locations would improve the coverage. As shown in Table 7, the percent decreases in detection probabilities due to background sources of ^{133}Xe are significant over large regions of the globe.

New generation noble gas samplers under development (Haas et al., 2017; TBE, 2020; Topin et al., 2020) and deployed in the IMS (Ringbom et al., 2017) and have lower detection levels and shorter sample collection periods than current systems. These new systems will improve the detection capabilities, especially in the number of detected samples.

4. Discussion

The results in this paper are based on atmospheric transport simulations that used 10 days of transport after the release events. These transport runs were performed in the reversed-time direction for computational convenience. Detection probabilities would likely increase, especially for larger magnitude releases, if longer transport times were used.

Using the values in Appendix 1, the average MDC of ^{131}I is 3.34 μBq/m^3, which is lower (better) than the average MDC of ^{140}Ba at 9.92 μBq/m^3. Thus, ^{131}I has a somewhat higher probability of being detected at low release magnitudes than ^{140}Ba. The average MDC for ^{133}Xe is much poorer at 0.231 mBq/m^3 (or 231 μBq/m^3), thus it has a lower probability of detecting smaller magnitude releases. However, the release of ^{133}Xe from a small underground nuclear explosion may be larger than the releases of ^{131}I or ^{140}Ba. In addition, atmospheric transport of ^{133}Xe is not affected by atmospheric loss processes, such as dry or wet deposition, that reduce the ^{131}I and ^{140}Ba concentrations.

The network performance for different release magnitudes of ^{140}Ba, ^{131}I, and ^{133}Xe is discussed in Sect. 4.1. The stations mode impacted by background are discussed in Sect. 4.2. In Sect. 4.3, a hypothetical release scenario is discussed that would combine data from the aerosol and noble gas networks. Finally, the implications of other background thresholds is discussed in Sect. 4.4.

4.1. Network Performance for Different Release Magnitudes of ^{140}Ba, ^{131}I, and ^{133}Xe

A summary of network performance for different release magnitudes of ^{140}Ba, ^{131}I, and ^{133}Xe is provided in Fig. 12 using current equipment detection characteristics that are influenced by background. Although results for iodine, barium, and xenon are shown on the same graph, the data in Table 1 suggest that their release magnitudes may be quite different in a real event.

The results shown in Fig. 12 cover 7 orders of magnitude of releases, from 10^6 to 10^{16} Bq. Using the rough scale that 1 kiloton of fission equals 10^{23} fission atoms, applying fission yields and a half-life

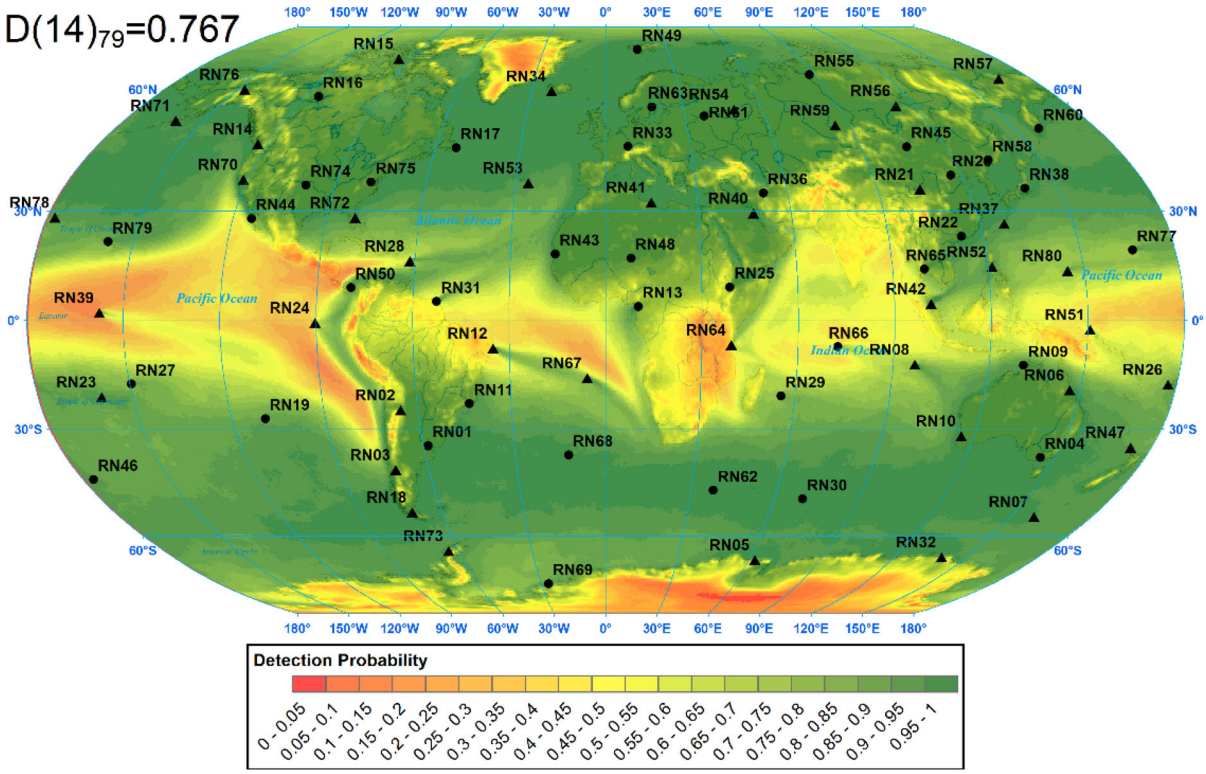
D(14)79=0.767
RN15
RN49
RN76
RN16
RN34
RN55
RN57
RN71
RN63
RN54
RN56
RN14
RN61
RN59
RN60
RN17
RN33
RN45
RN58
RN70
RN74
RN75
RN53
RN20
RN21
RN38
RN78
RN44
RN72
RN41
RN36
RN40
RN37
RN79
RN22
RN77
RN28
RN43
RN48
RN65
RN52
RN80
RN50
RN25
RN39
RN31
RN13
RN42
RN24
RN64
RN51
RN12
RN66
RN08
RN09
RN67
RN06
RN26
RN23
RN27
RN29
RN02
RN11
RN19
RN10
RN47
RN01
RN04
RN68
RN03
RN46
RN62
RN30
RN18
RN07
RN73
RN05
RN32
RN69
Pacific Ocean
Atlantic Ocean
Indian Ocean
Detection Probability
0 - 0.05
0.05 - 0.1
0.1 - 0.15
0.15 - 0.2
0.2 - 0.25
0.25 - 0.3
0.3 - 0.35
0.35 - 0.4
0.4 - 0.45
0.45 - 0.5
0.5 - 0.55
0.55 - 0.6
0.6 - 0.65
0.65 - 0.7
0.7 - 0.75
0.75 - 0.8
0.8 - 0.85
0.85 - 0.9
0.9 - 0.95
0.95 - 1

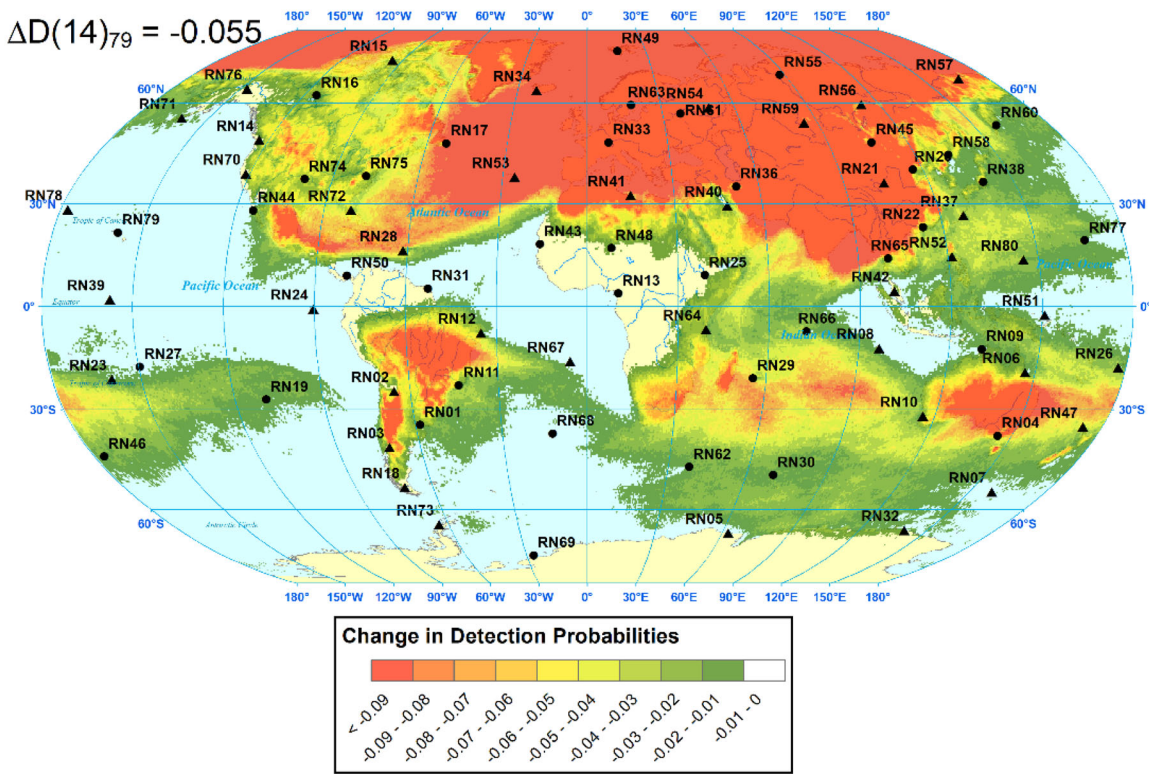
ΔD(14)79 = -0.055
RN15
RN49
RN76
RN16
RN34
RN55
RN57
RN71
RN63
RN54
RN56
RN14
RN61
RN59
RN60
RN17
RN33
RN45
RN58
RN70
RN74
RN75
RN53
RN20
RN21
RN38
RN78
RN44
RN72
RN41
RN36
RN40
RN37
RN79
RN22
RN77
RN28
RN43
RN48
RN65
RN52
RN80
RN50
RN25
RN39
RN31
RN13
RN42
RN24
RN64
RN51
RN12
RN66
RN08
RN09
RN67
RN06
RN26
RN23
RN27
RN29
RN02
RN11
RN19
RN10
RN47
RN01
RN04
RN68
RN03
RN46
RN62
RN30
RN18
RN07
RN73
RN05
RN32
RN69
Pacific Ocean
Atlantic Ocean
Indian Ocean
Change in Detection Probabilities
< -0.09
-0.09 - -0.08
-0.08 - -0.07
-0.07 - -0.06
-0.06 - -0.05
-0.05 - -0.04
-0.04 - -0.03
-0.03 - -0.02
-0.02 - -0.01
-0.01 - 0

◀Figure 11
Detection probabilities for a 79-station network for a 10^{14} Bq release of ^{133}Xe anywhere on the globe (upper pane). Change in the detection probability when the station detection limits are raised to an anomaly level equal to the 95th percentile of modeled background (lower pane)

of around a week, this scale can be roughly translated to covering the nuclear explosion yield in the atmosphere from 100 g to 1 kiloton. The low end of the magnitude range is included to show that a sparse network of current sensitivity has little chance of detecting an extremely small release, say, 10^{10} Bq or 1 kg equivalent explosion, unless the release were to occur close to a measurement system and directly upwind of it. At 10^{13} Bq release, which corresponds roughly to one-ton equivalent of fission in the atmosphere, the detection probabilities for aerosols are quite good ($\sim$ 75%) and for xenon are still considerable ($\sim$ 45%).

Estimates of releases from the Fukushima nuclear power plants in 2011 for ^{133}Xe (Eslinger et al., 2014a) and ^{131}I (Koo et al., 2014) of around 10^{19} Bq and 10^{17} Bq, respectively are larger than the upper end of the range in Fig. 12, perhaps corresponding to a megaton equivalent release of xenon and 10 kiloton equivalent release for iodine, and were detected all across the northern hemisphere (Biegalski et al., 2012). Of more interest, from a treaty monitoring perspective, is the ability to detect a test with a small yield, such as the tests conducted by the DPRK (Ringbom et al., 2009, 2014). The 2006 test yield was probably on the order of 1 kiloton (Murphy et al., 2013), while the yield of the 2013 test was a little larger in the 2.0–4.8 kiloton range (Murphy et al., 2013). Measured ^{133}Xe and ^{131m}Xe for the 2013 test suggest a release for both tests on the order of 10^{14} Bq of ^{133}Xe. No aerosol samples detected ^{131}I, so the release magnitude can be bounded, but not be estimated.

There are fewer industrial sources of ^{131}I than ^{133}Xe, although occasionally there are accidental releases, such as in Hungary in 2011 (Tichý et al., 2017), not at production facilities. Thus, as seen in Fig. 9, the background interference is regional in scope, with stations in China and the Russian

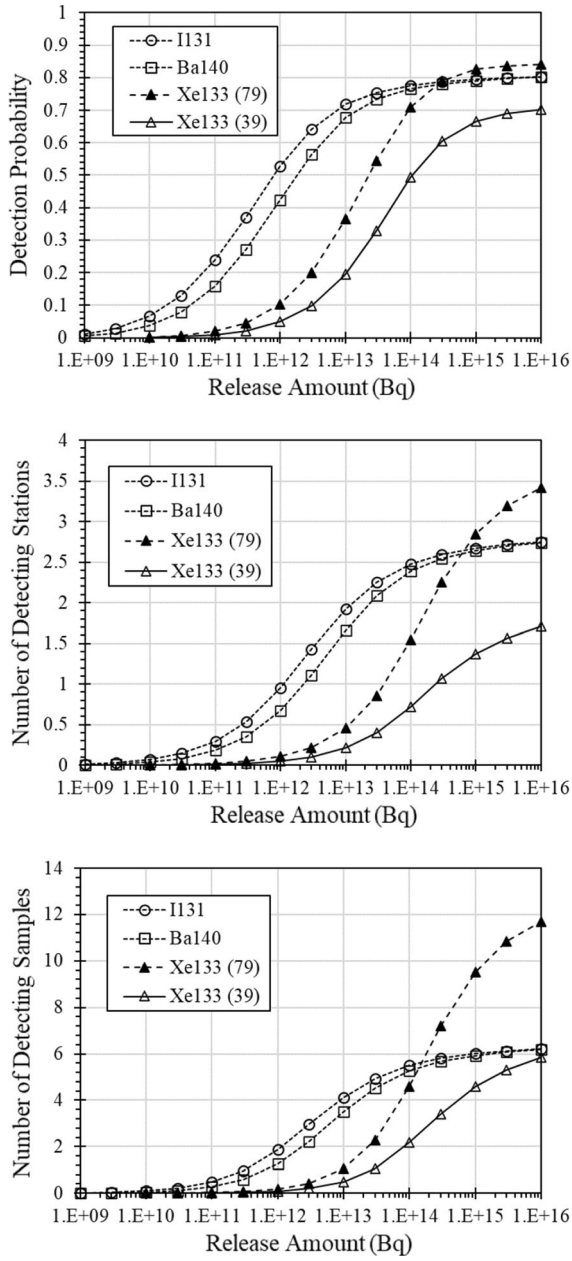

Figure 12
Summary of network performance for different magnitude releases of ^{140}Ba, ^{131}I, and ^{133}Xe using current equipment characteristics and measured or estimated background anomaly levels. The two curves for ^{133}Xe are for 39-station and 79-station networks. The detection probabilities, D(M), are shown in the top panel. The number of stations detecting the release, N(M), are shown in the middle panel. The number of samples detecting the release, S(M), are shown in the bottom panel. All results are for 10 days of atmospheric transport following the release event

Table 8

The 12 stations most impacted by the background concentrations of ^{133}Xe

Station	System MDC (mBq/m^3)	Median (mBq/m^3)	95th percentile (mBq/m^3)
RN61	0.5	0.531	50.1
RN54	0.5	0.446	44.7
RN33	0.15	0.221	36.7
RN57	0.5	4.850	20.7
RN21	0.15	0.464	19.3
RN59	0.5	0.081	9.73
RN04	0.2	0.000	9.53
RN63	0.2	0.182	8.26
RN49	0.2	0.001	7.25
RN20	0.15	0.097	7.23
RN01	0.5	0.166	7.07
RN55	0.5	0.003	6.58

Federation being most impacted. The estimated background for ^{133}Xe is global in scope, as seen in Fig. 11.

In the data in Table 6 for ^{131}I, and Table 7 for ^{133}Xe, the ΔD(M), ΔN(M), and ΔS(M) columns show that background interference degrades network performance more for small design basis magnitudes than for larger magnitudes. The tables also show that denser networks mitigate, to some extent, the degradation in detection performance from background emitters. However, network performance estimates need to rest on realistic release magnitudes. For example, analysis of data following the DPRK nuclear explosive test in 2013 yielded ^{133}Xe concentrations that would have been indistinguishable from background without the concurrent detection of ^{131m}Xe (Ringbom et al., 2014).

4.2. Stations Most Impacted by Background

The data given in Tables 9 and 10 show the background levels of ^{131}I and ^{133}Xe that impact each station. The data there can be used to rank the stations that are impacted the most by background. Table 4 shows the stations most impacted by background levels of ^{131}I. Table 8 shows the 12 stations most impacted by the background levels of ^{133}Xe. The stations are ranked by the 95th percentile anomaly level, but the median concentrations are also given. The median value is at or below the MDC for 7 of the 12 stations.

The number of stations reporting and the number of detecting samples are also important metrics and were not considered in WP.224. Along with all the other assumptions made to compute results shown here, a tacit assumption is that all stations are in good working order, and do not suffer power outages or other issues when needed. Thus, it could be considered crucial to have more than one station detecting. The lack of a second detecting station does not weaken any detection results obtained, but the network is more robust in multiplicity. Similarly, the number of detecting samples add confidence in the result. But multiple detections in time and space can be used with atmospheric transport modeling to limit the size of the region in which the signal originated (Eslinger & Schrom, 2016; Eslinger et al., 2019).

4.3. Hypothetical Release Scenario Combining Aerosol and Noble Gas Networks

It is probably unwise to make an assumption about how radioactive material will be released from an underground nuclear test: the release pathway through the geologic containment, if any, may include a complex of wet or dry fractures, while the engineered containment may include filled tunnels and sealed doorways. These could combine in many ways to produce the various results found in Schoengold et al. (1996), including frequently no measured release at all. But it can be enlightening to create a hypothetical release scenario that elucidates how the xenon and aerosol networks could work together.

Let us hypothesize a 1 kiloton equivalent nuclear explosion with a release of xenon similar to that described in Ringbom et al. (2009). In this scenario, about 1% of the ^{133}Xe would be released, or 10^{14} Bq, after 3 days of decay chain ingrowth. The reader can choose from Fig. 3 some combination of ingrowth time and containment suppression that achieves a 10^{14} Bq release. Ely et al. (2021) estimate for U.S. underground nuclear explosive tests that an average ^{131}I leakage would be about one part in 10^5 or less, but without a timing estimate for when the release

occurs. Using the approximation that 10^{23} radioactive atoms are created in a 1 kiloton test, a release fraction of 10^{-5} or slightly higher, the cumulative yield of ^{131}I from Table 1, and a decay constant on the order of 10^{-6} s^{-1}, one obtains an approximate 10^{11} Bq release of ^{131}I. In this scenario, there is only a factor of 1000 separating the activity of xenon and iodine.

If an explosion were to release 10^{14} Bq of ^{133}Xe and 10^{11} Bq of ^{131}I, then from Fig. 12, assuming 79-station networks for all samplers, the detection probability, D(14), is a very strong 0.76 for ^{133}Xe and D(11) is a poor, but not hopeless, 0.25 for ^{131}I. The number of samples with detections, S(11), is 0.52 for ^{131}I, but S(14) is a robust 6.4 for ^{133}Xe. By comparison, the DPRK nuclear explosive test in 2013 resulted in ^{133}Xe detections at 2 stations in a total of 5 ^{133}Xe detects (Ringbom et al., 2014), which adds some confidence that these modeling results are valid. Further, because D(11) for ^{131}I is only 25%, the lack of IMS measurement results cannot rule out the hypothetical release scenario.

Because the 79 noble gas systems have a much better chance of detecting a leaking test than the 79 aerosol systems, it might be tempting to wonder if the aerosol network is needed. If, however, there were half as many xenon systems, say 39 vs 79 and thus, half as many detecting xenon samples, adding one or two iodine detections would materially increase the confidence in the detection. If the MDC for ^{131}I were improved by an order of magnitude as suggested in Miley (2019), then for regions that do not have a serious ^{131}I background issue, D(M) could improve to 0.54 and S(M) could improve to 2.0. It has not been mentioned to this point that the IMS also contains a network of 16 laboratories for the confirmatory remeasurement of aerosol samplers. Several of these are equipped with ultra-low background detectors, and it has been shown that these can obtain an order of magnitude sensitivity increase for ^{131}I (Aalseth et al., 2009). This hypothetical scenario implies that sending the aerosol samples collected nearby the detecting xenon samples for ultra-low background measurement at IMS laboratories might yield additional evidence for or against the hypothesis that the source was a nuclear explosion.

While the scenario posited here is no more likely than others, it shows that the aerosol network plus its laboratories could substantially contribute to detecting small release underground nuclear test events now, and with station improvements, could make those contributions in near real-time. Another observation, without prejudice for the release mechanism, is that iodine, barium, and presumably other aerosols constitute a very sensitive detection means for small magnitude sources in the atmosphere that are orders of magnitude smaller than the detection measurement range of current xenon technology.

4.4. Other Possible Background Thresholds

If background estimates could be made sufficiently accurate, the 95th percentile could be adjusted temporally to lower the action threshold significantly. Approaches to accomplish this might include:

- Additional noble gas background measurement campaigns at IMS locations currently without a noble gas sampler. This would provide sampled data very useful for verifying and improving the modeled global concentrations. The change in network detection probabilities, ΔD(14), shown in Fig. 11 could be used to help select measurement locations with significant background concentrations.
- Besides IMS locations, the addition of local monitoring data, for example from local networks, safety systems, or stack monitors could greatly influence background calculations and potentially improve background estimates.

Another avenue of mitigation of the background radioactivity impact is to make the aerosol and xenon systems more supportive of each other. One order of magnitude additional iodine sensitivity in the aerosol network could allow ^{131}I detections to occur in support of xenon detections, raising the confidence and location capability of the combined network substantially. There are six stations on both the most impacted aerosol and xenon lists in Tables 4 and 8. These stations and the regions around them, RN01, RN20, RN21, RN54, RN59, and RN61, might be prime candidates for a noble gas background measurement campaign to understand the sources and find ways to improve the action threshold. Such a

field campaign could further help develop the concepts of fusion between aerosol and xenon networks.

Acknowledgements

The authors are grateful to Martin Kalinowski and Ted Bowyer for useful discussions. This paper describes objective technical results and analysis. The authors gratefully acknowledge the NOAA Air Resources Laboratory (ARL) for provision of the HYSPLIT transport and dispersion model used in this publication and the associated meteorological data. Any subjective views or opinions expressed in the paper do not necessarily represent the views of the U.S. Department of Energy or the United States Government.

Author Contributions All authors contributed to the study conception and design. The first draft of the manuscript was written by PWE and all authors commented on previous versions of the manuscript. All authors read and approved the final manuscript.

Funding

The National Nuclear Security Administration Defense Nuclear Nonproliferation Office of Nonproliferation and Arms Control funded this work. Pacific Northwest National Laboratory is operated under Contract DE-AC05-76RL01830 with the U.S. Department of Energy.

Declarations

Conflict of interest The authors have no relevant financial or non-financial interests to disclose.

Appendix 1: Additional Information about Detection Limits and Anomalous Background Levels

The operational data used to assign the detection limits for the four types of aerosol samplers in operation in the IMS are summarized in Table 9. Data to determine the average MDC values are obtained for 2 years (2019–2020) if the system regularly reported data. Two years is long enough to capture both daily and seasonal variations in ^{212}Pb backgrounds. Some stations were not in operation or collected a limited number of samples in 2019–2020, so the data period for them was extended to cover 2012–2020. Starting the data collection in 2012 means the ^{131}I released from the Fukushima nuclear power plants following the 2011 earthquake would have decayed away (Biegalski et al., 2012). In a desire to only include data where the sampler was operating properly, the following screening criteria were implemented on reviewed radionuclide reports (RRR): (a) the sample had a spectrum category of 1, 2, 3, 4, or 5, (b) the air flow-rate quality flag was 'PASS', (c) the acquisition time was between 20 and 28 h, and (d) the ^{212}Pb concentration was less than 400,000 μBq/m^3. For the 2012–2020 time period, approximately 200,000 samples met the screening criteria. The ^{131}I concentration data in Table 9 are for samples taken between January 1, 2012 and February 15, 2021.

Three types of noble gas samplers were deployed in the IMS at the time these calculations were performed. The SAUNA (Ringbom et al., 2003) has a 0.2 mBq/m^3 MDC for ^{133}Xe using 12-h samples. The next-generation Swedish system (Ringbom et al., 2017), denoted by SAUNA III, uses a 6 h collection period and began operation at IMS station RN63 in Stockholm, Sweden in the middle of 2021. The SAUNA III system is not used in this analysis. The SPALAX (Fontaine et al., 2004) has a 0.15 mBq/m^3 MDC for ^{133}Xe using 24-h samples. The ARIX (Dubasov et al., 2005) has a 0.5 mBq/m^3 MDC for ^{133}Xe using 12-h samples. Fortunately, the noble gas concentrations do not depend on the ^{212}Pb background. For this analysis, all noble gas samplers were assumed to have a 12-h collection period. The stations with a SPALAX sampler were assumed to have a detection limit of 0.15 for all samples.

Currently, only 40 of the radionuclide sampling locations in the treaty have noble gas samplers. That number is reduced to 39 because RN35 does not have specified coordinates in the treaty. Thus, some assumptions are required to model a 79-station noble gas network. The entries in Table 10 are based on three assignment rules for stations where noble gas systems are not currently installed: 1) If the same country operates a noble gas sampler at another location in the IMS, the same equipment is used.

Table 9

Information on the detection limits and ^{131}I detections used in the network performance analyses

Station ID	^{140}Ba MDC[a]	^{131}I MDC	Average ^{212}Pb conc	Number of samples	Data time period for MDCs	Number of ^{131}I detections	95th percentile of ^{131}I	Substitute station[b]
RN01	11.91	3.78	5.57×10^4	672	2019–2020	80	14.92	
RN02	9.35	2.84	NA	0	NA[c]	NA	NA	RN01, RN03
RN03	6.79	1.90	2.45×10^4	686	2019–2020	3		
RN04	12.34	3.67	1.00×10^5	710	2019–2020	3		
RN05	3.65	1.27	1.43×10^3	699	2019–2020	1		
RN06	14.51	4.47	1.42×10^5	586	2019–2020			
RN07	3.63	1.11	3.54×10^0	714	2019–2020	1		
RN08	4.07	1.46	2.43×10^0	709	2019–2020	1		
RN09	12.17	4.18	1.59×10^5	695	2019–2020			
RN10	13.42	4.47	1.63×10^5	661	2019–2020	2		
RN11	15.14	5.21	9.62×10^4	687	2019–2020	1		
RN12	15.14	5.21	NA	0	NA	NA	NA	RN11
RN13	12.46	4.11	1.24×10^5	2593	2012–2020	1		
RN14	4.27	1.38	1.58×10^4	713	2019–2020	1		
RN15	8.44	2.88	4.65×10^3	677	2019–2020			
RN16	3.50	1.12	1.00×10^4	721	2019–2020			
RN17	3.11	1.02	4.19×10^3	717	2019–2020	7	1.57	
RN18	9.37	3.20	9.42×10^3	709	2019–2020	3		
RN19	8.70	3.20	1.83×10^4	654	2019–2020	1		
RN20	14.20	4.81	1.40×10^5	459	2019–2020	145	16.92	
RN21	16.56	5.42	2.59×10^5	318	2019–2020	23	20.21	
RN22	15.40	5.19	1.83×10^5	419	2019–2020	224	23.35	
RN23	9.34	3.01	4.56×10^4	695	2019–2020			
RN24	10.28	3.68	4.16×10^3	663	2019–2020			
RN25	16.38	5.20	NA	0	NA	NA	NA	RN48
RN26	5.11	1.45	8.36×10^3	649	2019–2020			
RN27	14.01	4.52	3.12×10^4	3213	2012–2020	1		
RN28	5.56	1.93	8.74×10^3	712	2019–2020	1		
RN29	9.70	3.31	2.76×10^4	709	2019–2020	1		
RN30	6.59	2.15	9.71×10^3	2883	2012–2020			
RN31	7.95	2.67	2.01×10^4	710	2019–2020			
RN32	5.54	1.59	2.73×10^2	1319	2012–2020			
RN33	11.59	4.15	2.63×10^4	714	2019–2020			
RN34	8.60	2.78	2.08×10^3	641	2019–2020	3		
RN35	NA	NA	NA	NA	NA	NA	NA	
RN36	20.09	7.35	NA	0	NA	NA	NA	RN40
RN37	8.85	3.31	1.09×10^4	679	2019–2020	4		
RN38	12.28	4.34	3.30×10^4	643	2019–2020	1		
RN39	2.95	0.96	1.81×10^2	676	2019–2020			
RN40	20.09	7.35	0.973×10^4	653	2019–2020	6	7.55	
RN41	16.38	5.20	NA	0	NA	NA	NA	RN48
RN42	12.14	3.88	8.48×10^4	707	2019–2020	5		
RN43	9.05	3.10	6.64×10^4	2924	2012–2020	2		
RN44	16.56	5.91	NA	0	NA	NA	NA	RN70
RN45	17.84	5.80	1.04×10^5	3027	2012–2020			
RN46	3.47	1.06	5.86×10^3	695	2019–2020	3		
RN47	4.05	1.20	1.22×10^4	714	2019–2020			
RN48	16.38	5.20	2.54×10^5	346	2019–2020	1		
RN49	10.46	3.12	1.41×10^4	665	2019–2020	1		
RN50	4.34	1.54	6.72×10^3	711	2019–2020	41	3.68	
RN51	10.45	3.06	7.14×10^4	701	2019–2020	1		
RN52	5.91	1.98	1.36×10^4	645	2019–2020	79	4.21	
RN53	12.07	3.87	3.46×10^4	600	2019–2020			
RN54	5.72	2.00	1.73×10^4	2868	2012–2020	76	4.18	

Table 9 *continued*

Station ID	^{140}Ba MDC[a]	^{131}I MDC	Average ^{212}Pb conc	Number of samples	Data time period for MDCs	Number of ^{131}I detections	95th percentile of ^{131}I	Substitute station[b]
RN55	8.37	2.70	2.28×10^4	270	2019–2020			
RN56	5.09	1.74	1.07×10^4	635	2019–2020	7	1.11	
RN57	4.70	1.58	1.35×10^4	661	2019–2020			
RN58	12.31	4.11	1.18×10^5	3021	2012–2020	14	8.07	
RN59	9.24	3.12	7.72×10^4	2297	2012–2020	12	2.99	
RN60	3.85	1.36	1.36×10^3	2928	2012–2020			
RN61	6.81	2.34	3.06×10^4	692	2019–2020	449	29.85	
RN62	6.59	2.15	NA	0	NA	NA	NA	RN30
RN63	13.49	4.33	5.22×10^4	656	2019–2020	9	15.03	
RN64	5.67	2.00	2.36×10^4	668	2019–2020			
RN65	17.17	5.59	2.38×10^5	277	2019–2020	2		
RN66	8.33	2.95	5.31×10^2	703	2019–2020			
RN67	5.97	2.09	3.05×10^4	661	2019–2020			
RN68	3.18	1.14	1.87×10^3	705	2019–2020			
RN69	8.68	2.93	NA	0	NA	NA	NA	RN73
RN70	16.56	5.91	7.42×10^4	711	2019–2020	9	17.52	
RN71	7.13	2.39	2.04×10^3	714	2019–2020	2		
RN72	9.31	3.26	5.32×10^3	698	2019–2020	3		
RN73	8.68	2.93	7.22×10^2	694	2019–2020			
RN74	23.49	8.43	2.00×10^5	597	2019–2020			
RN75	16.17	5.75	7.50×10^4	711	2019–2020	1		
RN76	11.01	3.80	7.44×10^3	717	2019–2020			
RN77	7.15	2.61	2.36×10^2	653	2019–2020			
RN78	7.44	2.77	2.87×10^2	711	2019–2020	1		
RN79	9.93	3.57	9.37×10^3	717	2019–2020	1		
RN80	9.78	3.44	8.44×10^3	703	2019–2020	1		

[a]All MDCs and concentrations have units of μBq/m^3. The MDCs in this table are not adjusted for the concentration of ^{212}Pb

[b]Entry of a station ID means the ^{131}I and ^{140}Ba MDCs are assigned based on this adjacent station because no data are available for this treaty station. Entry of 2 station ID's means the average of two stations is used to assign the MDCs

[c]*NA* not applicable

These noble gas sampler assignments are denoted by using '()', for example, (SPALAX), 2) All other assignments use a SAUNA system, denoted by [SAUNA]. The SAUNA and SPALAX have nearly the same MDC for ^{133}Xe and the 12 h collection cycle matches with the assumptions in the underlying ATM analysis. New generation noble gas samplers under development (Haas et al., 2017; Ringbom et al., 2017; Topin et al., 2020) have lower detection levels and shorter sample collection periods than current systems. Although they are expected to have better network performance that the currently deployed systems, this work uses only the existing deployed sampler technologies.

Determining the anomalous detection level as the 95th percentile of detections is complicated by the fact that sampling data do not exist for many of the noble gas stations used in this analysis. Thus, the 95th percentile is based on modeling nominal release quantities for medical isotope production facilities and operating nuclear power plant complexes. We provide summary results in Table 10 followed by additional data on the source terms and a brief discussion of the modeling approach. The average fraction of the modeled concentrations due to medical isotope production facilities over the 2 years is also provided in Table 10. In most cases, the detections are dominated by MIPF releases.

The average daily release values of ^{133}Xe (Bq) for the 12 medical isotope production facilities used in this study are provided in Table 11. The release rates were compiled from published sources over the last 10 years, with no attempt to modify the published values in response to changing global production

Table 10

Information on the sampler type assignments and the ^{133}Xe anomaly limits (mBq/m^3) that will be compared with the sampler MDC

Gas station ID	Sampler technology	Noble gas status 2021[a]	Modeled 95th from MIPF and NPP	Average fraction from MIPF
RN01	ARIX	Installed	7.06×10^{0}	0.977
RN02	(ARIX)[b]	NA	5.28×10^{-2}	0.896
RN03	(ARIX)	NA	5.79×10^{-3}	0.903
RN04	SAUNA	Certified	9.53×10^{0}	1.000
RN05	(SAUNA)	NA	5.59×10^{-5}	0.994
RN06	(SAUNA)	NA	1.14×10^{0}	1.000
RN07	(SAUNA)	NA	2.22×10^{-1}	1.000
RN08	(SAUNA)	NA	2.39×10^{-2}	0.999
RN09	(SAUNA)	Certified	2.78×10^{-1}	1.000
RN10	(SAUNA)	NA	4.32×10^{-3}	0.998
RN11	SAUNA	Certified	1.34×10^{-1}	0.051
RN12	(SAUNA)	NA	4.43×10^{-6}	0.130
RN13	SPALAX	Certified	0.00×10^{0}	0.927
RN14	(SPALAX)	NA	3.65×10^{-3}	0.066
RN15	(SPALAX)	NA	3.48×10^{-3}	0.655
RN16	SPALAX	Certified	8.73×10^{-4}	0.222
RN17	SPALAX	Certified	1.45×10^{-1}	0.502
RN18	(SAUNA)	NA	1.55×10^{-3}	0.961
RN19	SAUNA	Certified	2.43×10^{-3}	1.000
RN20	SPALAX	Installed	7.22×10^{0}	0.983
RN21	(SPALAX)	NA	1.93×10^{1}	0.999
RN22	SPALAX	Installed	1.55×10^{0}	0.324
RN23	(SAUNA)	NA	1.21×10^{-2}	1.000
RN24	(SAUNA)	NA	0.00×10^{0}	0.000
RN25	[SAUNA][c]	Planned	4.92×10^{-4}	0.135
RN26	[SAUNA]	NA	6.72×10^{-2}	1.000
RN27	SPALAX	Certified	0.00×10^{0}	1.000
RN28	(SPALAX)	NA	3.52×10^{-5}	0.145
RN29	SPALAX	Certified	3.16×10^{-1}	1.000
RN30	SPALAX	Certified	1.56×10^{-1}	0.999
RN31	SPALAX	Certified	0.00×10^{0}	0.000
RN32	(SPALAX)	NA	1.66×10^{-3}	0.999
RN33	SPALAX	Certified	3.47×10^{1}	0.776
RN34	[SAUNA]	NA	7.72×10^{-1}	0.945
RN35	NA	NA	NA	NA
RN36	[SAUNA]	Planned	5.51×10^{-1}	0.617
RN37	(SAUNA)	NA	3.72×10^{-1}	0.714
RN38	SAUNA	Certified	3.67×10^{-1}	0.000
RN39	[SAUNA]	NA	0.00×10^{0}	0.921
RN40	[SAUNA]	NA	3.06×10^{-1}	0.932
RN41	[SAUNA]	NA	2.89×10^{0}	0.868
RN42	[SAUNA]	NA	7.21×10^{-2}	0.916
RN43	[SAUNA]	Planned	1.30×10^{-2}	0.006
RN44	SAUNA	Certified	2.46×10^{-3}	0.992
RN45	SPALAX	Certified	1.90×10^{0}	1.000
RN46	SAUNA	Certified	6.51×10^{-1}	1.000
RN47	(SAUNA)	NA	6.96×10^{-1}	0.876
RN48	[SAUNA]	Planned	3.31×10^{-2}	0.980
RN49	SAUNA	Certified	6.98×10^{0}	0.001
RN50	SPALAX	Certified	7.18×10^{-6}	1.000
RN51	[SAUNA]	NA	2.85×10^{-5}	0.755
RN52	[SAUNA]	NA	7.36×10^{-2}	0.894
RN53	[SAUNA]	NA	1.22×10^{-1}	0.996
RN54	(ARIX)	NA	4.47×10^{1}	0.995
RN55	(ARIX)	Planned	6.58×10^{0}	0.996

Table 10 *continued*

Gas station ID	Sampler technology	Noble gas status 2021[a]	Modeled 95th from MIPF and NPP	Average fraction from MIPF
RN56	(ARIX)	NA	4.41×10^{0}	0.001
RN57	(ARIX)	NA	2.75×10^{1}	0.882
RN58	ARIX	Installed	7.93×10^{-1}	0.996
RN59	(ARIX)	NA	9.72×10^{0}	0.818
RN60	ARIX	Installed	2.53×10^{-2}	0.986
RN61	ARIX	Installed	5.01×10^{1}	0.999
RN62	[SAUNA]	Planned	7.17×10^{-2}	0.907
RN63	SAUNA	Certified	8.16×10^{0}	1.000
RN64	[SAUNA]	NA	7.36×10^{-1}	0.631
RN65	[SAUNA]	Planned	1.18×10^{-1}	0.740
RN66	SAUNA	Certified	2.79×10^{-3}	0.992
RN67	(SAUNA)	NA	1.57×10^{-3}	0.875
RN68	SAUNA	Certified	4.72×10^{-3}	0.992
RN69	(SAUNA)	Planned	8.49×10^{-5}	0.057
RN70	(SAUNA)	NA	2.41×10^{-3}	0.713
RN71	(SAUNA)	NA	3.16×10^{-3}	0.017
RN72	(SAUNA)	NA	1.08×10^{-1}	0.968
RN73	(SAUNA)	NA	2.45×10^{-6}	0.056
RN74	SAUNA	Certified	2.59×10^{-2}	0.036
RN75	SAUNA	Certified	2.17×10^{-1}	0.276
RN76	(SAUNA)	NA	3.07×10^{-3}	0.796
RN77	SAUNA	Certified	9.87×10^{-3}	0.779
RN78	(SAUNA)	NA	3.23×10^{-2}	0.709
RN79	SAUNA	Certified	2.72×10^{-3}	0.740
RN80	(SAUNA)	NA	3.17×10^{-3}	0.000

[a]Status checked on April 1, 2021 at website https://www.ctbto.org/verification-regime/station-profiles/

[b]Entries in '()' are assigned because the same country operates that type of sampler

[c]Entries in '[]' are assigned a SAUNA sampler

Table 11

Daily release rates of ^{133}Xe (Bq) used for each medical isotope production facility

Facility	Country	Release	References
CNEA Ezeiza	Argentina	1.64×10^{10}	Carranza et al. (2013)
ANSTO	Australia	1.86×10^{12}	Schöppner et al. (2013)
INST	Bangladesh	2.74×10^{10}	IAEA (2016)
IRE	Belgium	2.74×10^{12}	Saey (2009)
HFETR	China	1.00×10^{12}	Achim et al. (2016)
BATAN	Indonesia	3.72×10^{11}	Tinker et al. (2010)
Covidien	Netherlands	2.00×10^{9}	Saey (2009)
NIIAR	Russian Federation	5.51×10^{12}	IAEA (2012)
Karpov Institute	Russian Federation	8.25×10^{11}	Vakulovskii and Kryshev (2005)
NECSA	South Africa	1.12×10^{13}	Saey (2009)
PINSTECH	Pakistan	1.00×10^{12}	Mushtaq et al. (2012)
Nordion	Canada	4.11×10^{10}	WOSMIP (2017)

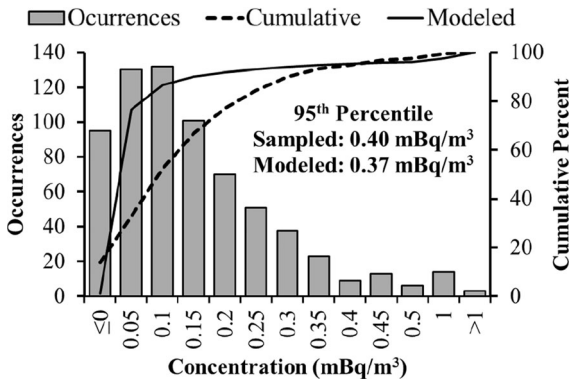

Figure 13
Comparison of measured ^{133}Xe concentrations for 2019 at RN38 (Takasaki, Japan) with modeled concentrations based on nominal releases from nuclear power plants and medical isotope production facilities

levels of ^{99m}Tc. However, the facility at Chalk River, Canada, has ceased operations and was not included in this study. In some cases, such as PINSTECH in Pakistan, the release rate was estimated using announced production rates of ^{99m}Tc, combined with basic knowledge of the type of separations technology used in the facility.

Daily release estimates were developed for the nuclear power plants in the online Power Reactor Information System (IAEA-PRIS, 2019) that were operating in 2019. These nuclear power plants are operating at 181 different locations. All release rates were set to 4.67×10^9 Bq/d per reactor, which is derived from the combined continuous and batch releases (arithmetic average) in Table 4 of Kalinowski and Tuma (2009). Releases at each location accounted for the number of operating reactors. Many of the locations have only one reactor, but others have multiple reactors. For example, the Qinshan complex in China has 7 operating reactors.

The atmospheric transport runs in the Hysplit code (Stein et al., 2015) that propagate facility emissions of ^{133}Xe used archived meteorological data for 2015 and 2016 on a 0.5° spacing and 3-h time step (GDAS0P5, 2020). Each run modeled plume movement for 10 days after release and saved concentration data for each hour on a global 0.25° grid. The concentration data were then interpolated to individual sampler locations and aggregated to the sampler collection time periods.

A comparison of modeled versus measured ^{133}Xe values for 2019 at the IMS station RN38 in Takasaki, Japan, is provided in Fig. 13. The model predicts more values below about 0.25 mBq/m^3 than are measured, but the cumulative frequency of predictions and measured values is quite close for values of 0.35 or higher. The sampled data are not censored below the detection limit of approximately 0.25 mBq/m^3. The 95th percentiles agree quite nicely, providing evidence that the 95th percentile anomaly level based on the modeled concentrations is reasonable.

References

Aalseth, C., Andreotti, E., Arnold, D., Cabeza, J.-A.S., Degering, D., Giuliani, A., de Orduña, R. G., Gurriaran, R., Hult, M., Keillor, M., Laubenstein, M., le Petit, G., Margineanu, R. M., Matthews, K. M., Miley, H., et al. (2009). Ultra-low background measurements of decayed aerosol filters. *Journal of Radioanalytical and Nuclear Chemistry, 282*(3), 731–735. https://doi.org/10.1007/s10967-009-0307-0

Achim, P., Generoso, S., Morin, M., Gross, P., Le Petit, G., & Moulin, C. (2016). Characterization of Xe-133 global atmospheric background: Implications for the International Monitoring System of the Comprehensive Nuclear-Test-Ban Treaty. *Journal of Geophysical Research: Atmospheres, 121*(9), 4951–4966. https://doi.org/10.1002/2016JD024872

Biegalski, S. R., Bowyer, T. W., Eslinger, P. W., Friese, J. A., Greenwood, L. R., Haas, D. A., Hayes, J. C., Hoffman, I., Keillor, M., Miley, H. S., & Moring, M. (2012). Analysis of Data from Sensitive U.S. Monitoring Stations for the Fukushima Daiichi Nuclear Reactor Accident. *Journal of Environmental Radioactivity, 114*, 15–21. https://doi.org/10.1016/j.jenvrad.2011.11.007

Bowyer, T. W., Kephart, R., Eslinger, P. W., Friese, J. I., Miley, H. S., & Saey, P. R. J. (2013). Maximum reasonable radioxenon releases from medical isotope production facilities and their effect on monitoring nuclear explosions. *Journal of Environmental Radioactivity, 115*(1), 192–200. https://doi.org/10.1016/j.jenvrad.2012.07.018

Carranza, E. C., Cristini, P., Novello, A., Bronca, M., Bavaro, R., Cestau, D., et al. (2013). Methods of retention and separation of hydrogen and noble gases generated in the dissolution of aluminum–uranium targets. *Workshop on Signatures of Medical and Industrial Isotope Production (WOSMIP IV)* (Nov. 11–13, 2013). Vienna, Austria (Unpublished presentation)

Chernov, M. Y., Ergashev, D. E., Gerasimchuk, O. A., Goryacheva, N. P., Molodtsev, D. A., Orlov, M. S., Probylov, V. V., Sidorov, N. A., Timofeev, D. V., & Tkachev, O. V. (2021). Upgrading the Detection System of the MIKS Xenon Isotope Monitoring Complex during Preparation for the International Certification, SnT 2021: CTBT Science and Technology Conference, Vienna, Austria

Clayson, C. A., & Kantha, L. (2008). On turbulence and mixing in the free atmosphere inferred from high-resolution soundings. *Journal of Atmospheric and Oceanic Technology, 25*(6), 833–852. https://doi.org/10.1175/2007JTECHA992.1

Comprehensive Nuclear-Test-Ban Treaty. (1996). *Text of the Comprehensive Nuclear-Test-Ban Treaty*. United Nations Office for Disarmament Affairs (UNODA), Status of Multilateral Arms Regulation and Disarmament Agreements, CTBT. http://www.ctbto.org/the-treaty/treaty-text/. Accessed 20 Sept 2012.

Croff, A. G. (1980). ORIGEN2: A revised and updated version of the Oak Ridge isotope generation and depletion code, ORNL-5621, Oak Ridge National Laboratory, Oak Ridge, TN. https://doi.org/10.2172/5352089.

CTBTO PrepCom. (2019). *Verification Regime*. http://www.ctbto.org/verification-regime/. Accessed 27 Feb 2019.

CTBTO PrepCom. (2020). *Verification Regime: Station Profiles*. https://www.ctbto.org/verification-regime/station-profiles/. Accessed 2 June 2020.

Currie, L. A. (1968). Limits for qualitative detection and quantitative determination: Application to radiochemistry. *Analytical Chemistry, 40*(3), 586–593. https://doi.org/10.1021/ac60259a007

Draxler, R. R., Stunder, B., Rolph, G., Stein, A., & Taylor, A. (2020). HYSPLIT4 User's Guide, Air Resources Laboratory, National Oceanic and Atmospheric Administration (NOAA), Silver Spring, Maryland. https://www.arl.noaa.gov/documents/reports/hysplit_user_guide.pdf. Accessed Sept 2020

Dubasov, Y. (2010). Underground nuclear explosions and release of radioactive noble gases. *Pure and Applied Geophysics, 167*(4), 455–461. https://doi.org/10.1007/s00024-009-0026-z

Dubasov, Y. V., Popov, Y. S., Prelovskii, V. V., Donets, A. Y., Kazarinov, N. M., Mishurinskii, V. V., Popov, V. Y., Rykov, Y. M., & Skirda, N. V. (2005). The АРИК-01 automatic facility for measuring concentrations of radioactive xenon isotopes in the atmosphere. *Instruments and Experiment Techniques, 48*(3), 373–379. https://doi.org/10.1007/s10786-005-0065-3

Ely, J., Fast, J., Seifert, C., & Warren, G. (2021). Estimation of ground-level radioisotope distributions for underground nuclear test leakage, PNNL-31135, Pacific Northwest National Laboratory, Richland, Washington

England, T., & Rider, B. (1994). Evaluation and Compilation of Fission Product Yields 1993, LA-UR-94-3106 (ENDF-349), Los Alamos National Laboratory, Los Alamos, New Mexico. http://t2.lanl.gov/nis/publications/endf349.pdf. Accessed Oct 2019

Eslinger, P. W., Biegalski, S. R., Bowyer, T. W., Cooper, M. W., Haas, D. A., Hayes, J. C., Hoffman, I., Korpach, E., Yi, J., Miley, H. S., Rishel, J. P., Ungar, K., White, B., & Woods, V. T. (2014). Source term estimation of radioxenon released from the Fukushima Dai-ichi nuclear reactors using measured air concentrations and atmospheric transport modeling. *Journal of Environmental Radioactivity, 127*(1), 127–132. https://doi.org/10.1016/j.jenvrad.2013.10.013

Eslinger, P. W., Lowrey, J. D., Miley, H. S., Rosenthal, W. S., & Schrom, B. T. (2019). Source term estimation using multiple xenon isotopes in atmospheric samples. *Journal of Environmental Radioactivity, 204*, 111–116. https://doi.org/10.1016/j.jenvrad.2019.04.004

Eslinger, P. W., Napier, B. A., & Anspaugh, L. R. (2014). Representative doses to members of the public from atmospheric releases of ^{131}I at the Mayak Production Association facilities from 1948 through 1972. *Journal of Environmental Radioactivity, 135*(2014), 44–53. https://doi.org/10.1016/j.jenvrad.2014.04.003

Eslinger, P. W., & Schrom, B. T. (2016). Multi-detection events, probability density functions, and reduced location area. *Journal of Radioanalytical and Nuclear Chemistry, 307*(3), 1599–1605. https://doi.org/10.1007/s10967-015-4339-3

Eslinger, P. W., & Schrom, B. T. (2019). Utility of atmospheric transport runs done backwards in time for source term estimation. *Journal of Environmental Radioactivity, 203*, 98–106. https://doi.org/10.1016/j.jenvrad.2019.03.006

Fitzgerald, J. W. (1975). Approximation formulas for the equilibrium size of an aerosol particle as a function of its dry size and composition and the ambient relative humidity. *Journal of Applied Meteorology, 14*(6), 1044–1049. https://doi.org/10.1175/1520-0450(1975)014%3c1044:afftes%3e2.0.co;2

Fontaine, J. P., Pointurier, F., Blanchard, X., & Taffary, T. (2004). Atmospheric xenon radioactive isotope monitoring. *Journal of Environmental Radioactivity, 72*(1–2), 129–135. https://doi.org/10.1016/S0265-931X(03)00194-2

GDAS0P5. (2020). *Global data assimilation system archive*. Air Resources Laboratory, National Oceanic and Atmospheric Administration. ftp://arlftp.arlhq.noaa.gov/pub/archives/gdas0p5/. Accessed 3 June 2020.

GDAS1. (2020). *Global data assimilation system archive*. Air Resources Laboratory, National Oceanic and Atmospheric Administration. ftp://arlftp.arlhq.noaa.gov/pub/archives/gdas1/. Accessed 3 June 2020.

Goorley, T., James, M., Booth, T., Brown, F., Bull, J., Cox, L. J., Durkee, J., Elson, J., Fensin, M., Forster, R. A., Hendricks, J., Hughes, H. G., Johns, R., Kiedrowski, B., Martz, R., et al. (2012). Initial MCNP6 release overview. *Nuclear Technology, 180*(3), 298–315. https://doi.org/10.13182/NT11-135

Gründel, M., Kopka, B., & Schulz, R. (2008). ^{131}I exhalation by patients undergoing therapy of thyroid diseases. *Radiation Protection Dosimetry, 129*(4), 435–438. https://doi.org/10.1093/rpd/ncm459

Gueibe, C., Kalinowski, M. B., Baré, J., Gheddou, A., Krysta, M., & Kusmierczyk-Michulec, J. (2017). Setting the baseline for estimated background observations at IMS systems of four radioxenon isotopes in 2014. *Journal of Environmental Radioactivity, 178–179*, 297–314. https://doi.org/10.1016/j.jenvrad.2017.09.007

Haas, D. A., Eslinger, P. W., Bowyer, T. W., Cameron, I. M., Hayes, J. C., Lowrey, J. D., & Miley, H. S. (2017). Improved performance comparisons of radioxenon systems for low level releases in nuclear explosion monitoring. *Journal of Environmental Radioactivity, 178–179*(2017), 127–135. https://doi.org/10.1016/j.jenvrad.2017.08.005

Hayes, J. C., Ely, J. H., Haas, D. A., Harper, W. W., Heimbigner, T. R., Hubbard, C. W., Humble, P. H., Madison, J. C., Morris, S. J., Panisko, M. E., Ripplinger, M. D., & Stewart, T. L. (2013). Requirements for Xenon International, PNNL-22227 Rev.1, Pacific Northwest National Laboratory, Richland, Washington. https://doi.org/10.2172/1122330

Hoffman, I., & Berg, R. (2018). Medical isotope production, research reactors and their contribution to the global xenon background. *Journal of Radioanalytical and Nuclear Chemistry*. https://doi.org/10.1007/s10967-018-6128-2

Hourdin, F., & Talagrand, O. (2006). Eulerian backtracking of atmospheric tracers. I: Adjoint derivation and parametrization of subgrid-scale transport. *Quarterly Journal of the Royal Meteorological Society, 132*(615), 567–583. https://doi.org/10.1256/qj.03.198.A

Hourdin, F., Talagrand, O., & Idelkadi, A. (2006). Eulerian backtracking of atmospheric tracers. II: Numerical aspects. *Quarterly Journal of the Royal Meteorological Society, 132*(615), 585–603. https://doi.org/10.1256/qj.03.198.B

IAEA. (2012). Meeting Report: Technical Meeting on Conversion Planning for Mo99 Production Facilities from HEU to LEU (IAEA Headquarters, 6–7 November, 2012). http://www.iaea.org/OurWork/ST/NE/NEFW/Technical_Areas/RRS/documents/mo99/2012TM_Meeting_Report.pdf. Accessed 23 Aug 2013.

IAEA. (2016). How Bangladesh is breaking down barriers to nuclear medicine. https://www.iaea.org/newscenter/news/how-bangladesh-is-breaking-down-barriers-to-nuclear-medicine. Accessed 2 June 2020.

IAEA-PRIS. (2019). Power Reactor Information System (IAEA-PRIS database). International Atomic Energy Agency, Vienna, Austria, http://www.iaea.org/pris/, http://www.iaea.org/pris/. Accessed Oct 2019

IMS Expert Group. (1995). International Monitoring System Expert Group Report based on Technical Discussions held from 6 February to 3 March 1995, Conference on Disarmament. United Nations, Geneva, Switzerland, p. 97, https://digitallibrary.un.org/record/205422/files/CD_NTB_WP.224-EN.pdf. Accessed Oct 2019

Kalinowski, M. (2001). Atmospheric transport modelling related to radionuclide monitoring in support of Comprehensive Nuclear-Test-Ban Treaty verification. *Kerntechnik-Bilingual Edition, 66*(3), 129–133, https://www.researchgate.net/profile/Martin-Kalinowski-2/publication/295793789_Atmospheric_transport_modelling_related_to_radionuclide_monitoring_in_support_of_the_Comprehensive_Nuclear-Test-Ban_Treaty_verification/links/570d5f7808ae3199889bbf53/Atmospheric-transport-modelling-related-to-radionuclide-monitoring-in-support-of-the-Comprehensive-Nuclear-Test-Ban-Treaty-verification.pdf

Kalinowski, M. B., & Tatlisu, H. (2020). Global radioxenon emission inventory from nuclear power plants for the calendar year 2014. *Pure and Applied Geophysics*. https://doi.org/10.1007/s00024-020-02579-w

Kalinowski, M. B., & Tuma, M. P. (2009). Global radioxenon emission inventory based on nuclear power reactor reports. *Journal of Environmental Radioactivity, 100*(1), 58–70. https://doi.org/10.1016/j.jenvrad.2008.10.015

Koo, Y.-H., Yang, Y.-S., & Song, K.-W. (2014). Radioactivity release from the Fukushima accident and its consequences: A review. *Progress in Nuclear Energy, 74*, 61–70. https://doi.org/10.1016/j.pnucene.2014.02.013

Maceira, M., Blom, P. S., MacCarthy, J. K., Marcillo, O. E., Euler, G. G., Begnaud, M. L., Ford, S. R., Pasyanos, M. E., Orris, G. J., Foxe, M. P., Arrowsmith, S. J., Merchant, B. J., & Slinkard, M. E. (2017). Trends in nuclear explosion monitoring research & development-a physics perspective, LA-UR-17-21274, Los Alamos National Labatory, Los Alamos, NM (United States). https://doi.org/10.2172/1355758

Miley, H. S., Eslinger, P. W., & Friese, J. I. (2021). Examining nuisance aerosol detections in light of the origin of the screening process, PNNL-SA-32446, Pacific Northwest National Laboratory, Richland, Washington. https://doi.org/10.2172/1843271

Miley, H., Bowyer, S., Hubbard, C., McKinnon, A., Perkins, R., Thompson, R., & Warner, R. (1998). A description of the DOE radionuclide aerosol sampler/analyzer for the Comprehensive Test Ban Treaty. *Journal of Radioanalytical and Nuclear Chemistry, 235*(1–2), 83–87. https://doi.org/10.1007/BF02385942

Miley, H. S., Burnett, J. L., Chepko, A. B., Devoy, C. L., Eslinger, P. W., Forrester, J. B., Friese, J. I., Lidey, L. S., Morris, S. J., Schrom, B. T., Stokes, S., Swanwick, M. E., Smart, J. E., & Warren, G. A. (2019). Design considerations for future radionuclide aerosol monitoring systems. *Journal of Environmental Radioactivity, 208–209*, 106037. https://doi.org/10.1016/j.jenvrad.2019.106037

Murphy, J., Stevens, J., Kohl, B., & Bennett, T. (2013). Advanced seismic analyses of the source characteristics of the 2006 and 2009 North Korean nuclear tests. *Bulletin of the Seismological Society of America, 103*(3), 1640–1661. https://doi.org/10.1785/0120120194

Mushtaq, A., Pervez, S., Hussain, S., Mirza, J. A., Khan, M. M., Asif, M., Siddique, M. U., Khalid, U., Khan, B., & Khalid, M. (2012). Evaluation of Pakgen ^{99m}Tc generators loaded with indigenous fission ^{99}Mo. *Radiochimica Acta, 100*(10), 793–801. https://doi.org/10.1524/ract.2012.1945

Rao, K. S. (2007). Source estimation methods for atmospheric dispersion. *Atmospheric Environment, 41*(33), 6964–6973. https://doi.org/10.1016/j.atmosenv.2007.04.064

Ringbom, A., Aldener, M., Axelsson, A., Fritioff, T., Kastlander, J., Mortsell, A., & Olsson, H. (2017). Analysis of data from an intercomparison between a Sauna II and a Sauna III system, Science and Technology 2017 Conference, Vienna, Austria, https://ctnw.ctbto.org/DMZ/abstract/21838. Accessed Oct 2019

Ringbom, A., Axelsson, A., Aldener, M., Auer, M., Bowyer, T. W., Fritioff, T., Hoffman, I., Khrustalev, K., Nikkinen, M., Popov, V., Popov, Y., Ungar, K., & Wotawa, G. (2014). Radioxenon detections in the CTBT international monitoring system likely related to the announced nuclear test in North Korea on February 12, 2013. *Journal of Environmental Radioactivity, 128*, 47–63. https://doi.org/10.1016/j.jenvrad.2013.10.027

Ringbom, A., Elmgren, K., Lindh, K., Peterson, J., Bowyer, T. W., Hayes, J. C., McIntyre, J. I., Panisko, M., & Williams, R. (2009). Measurements of radioxenon in ground level air in South Korea following the claimed nuclear test in North Korea on October 9, 2006. *Journal of Radioanalytical and Nuclear Chemistry, 282*(3), 773–779. https://doi.org/10.1007/s10967-009-0271-8

Ringbom, A., Larson, T., Axelsson, A., Elmgren, K., & Johansson, C. (2003). SAUNA—A system for automatic sampling, processing, and analysis of radioactive xenon. *Nuclear Instruments and Methods, 508*(3), 542–553. https://doi.org/10.1016/s0168-9002(03)01657-7

Saey, P. R. J. (2009). The influence of radiopharmaceutical isotope production on the global radioxenon background. *Journal of Environmental Radioactivity, 100*(5), 396–406. https://doi.org/10.1016/j.jenvrad.2009.01.004

Saey, P. R. J., Auer, M., Becker, A., Hoffmann, E., Nikkinen, M., Ringbom, A., Tinker, R., Schlosser, C., & Sonck, M. (2010). The influence on the radioxenon background during the temporary suspension of operations of three major medical isotope production facilities in the Northern Hemisphere and during the start-up of another facility in the Southern Hemisphere. *Journal of Environmental Radioactivity, 101*(9), 730–738. https://doi.org/10.1016/j.jenvrad.2010.04.016

Saey, P. R. J., Bowyer, T. W., & Ringbom, A. (2010). Isotopic noble gas signatures released from medical isotope production facilities—Simulations and measurements. *Applied Radiation and Isotopes, 68*(9), 1846–1854. https://doi.org/10.1016/j.apradiso.2010.04.014

Schoengold, C., DeMarre, M., & Kirkwood, E., (1996). Radiological effluents released from US continental tests, 1961 through 1992. Revision 1, Bechtel Nevada Corp., https://www.nnss.gov/docs/docs_LibraryPublications/DOENV_317.pdf

Schoeppner, M., & Plastino, W. (2014). Determination of the global coverage of the IMS Xenon-133 component for the detection of nuclear explosions. *Science & Global Security, 22*(3), 209–234. https://doi.org/10.1080/08929882.2014.952581

Schöppner, M., Plastino, W., Hermanspahn, N., Hoffmann, E., Kalinowski, M., Orr, B., & Tinker, R. (2013). Atmospheric transport modelling of time resolved ^{133}Xe emissions from the isotope production facility ANSTO, Australia. *Journal of Environmental Radioactivity, 126*(2013), 1–7. https://doi.org/10.1016/j.jenvrad.2013.07.003

Schulze, J., Auer, M., & Werzi, R. (2000). Low level radioactivity measurement in support of the CTBTO. *Applied Radiation and Isotopes, 53*(1), 23–30. https://doi.org/10.1016/S0969-8043(00)00182-2

Seibert, P., & Frank, A. (2004). Source-receptor matrix calculation with a Lagrangian particle dispersion model in backward mode. *Atmospheric Chemistry and Physics, 4*(1), 51–63. https://doi.org/10.5194/acp-4-51-2004

Stein, A. F., Draxler, R. R., Rolph, G. D., Stunder, B. J. B., Cohen, M. D., & Ngan, F. (2015). NOAA's HYSPLIT atmospheric transport and dispersion modeling system. *Bulletin of the American Meteorological Society, 96*(12), 2059–2077. https://doi.org/10.1175/BAMS-D-14-00110.1

Stocki, T. J., Armand, P., Heinrich, P., Ungar, R. K., D'Amours, R., Korpach, E. P., Bellivier, A., Taffary, T., Malo, A., Bean, M., Hoffman, I., & Jean, M. (2008). Measurement and modelling of radioxenon plumes in the Ottawa Valley. *Journal of Environmental Radioactivity, 99*(11), 1775–1788. https://doi.org/10.1016/j.jenvrad.2008.07.009

Stohl, A., Eckhardt, S., Forster, C., James, P., Spichtinger, N., & Seibert, P. (2002). A replacement for simple back trajectory calculations in the interpretation of atmospheric trace substance measurements. *Atmospheric Environment, 36*(29), 4635–4648. https://doi.org/10.1016/S1352-2310(02)00416-8

TBE. (2020). Xenon International Website at Teledyne Brown Engineering. https://tbe.com/energy/xenon-international. Accessed 22 Sept 2020.

Tichý, O., Šmídl, V., Hofman, R., Šindelářová, K., Hýža, M., & Stohl, A. (2017). Bayesian inverse modeling and source location of an unintended I-131 release in Europe in the fall of 2011. *Atmospheric Chemistry and Physics, Discussions, 2017*, 1–24. https://doi.org/10.5194/acp-2017-206

Tinker, R., Orr, B., Grzechnik, M., Hoffmann, E., Saey, P., & Solomon, S. (2010). Evaluation of radioxenon releases in Australia using atmospheric dispersion modelling tools. *Journal of Environmental Radioactivity, 101*(5), 353–361. https://doi.org/10.1016/j.jenvrad.2010.02.003

Topin, S., Gross, P., Achim, P., Generoso, S., Cagniant, A., Delaune, O., Morin, M., Philippe, T., Fontaine, J.-P., Moulin, C., Douysset, G., & Le Petit, G. (2020). 6 months of radioxenon detection in western Europe with the SPALAX-New generation system—Part1: Metrological capabilities. *Journal of Environmental Radioactivity, 225*, 106442. https://doi.org/10.1016/j.jenvrad.2020.106442

Vakulovskii, S. M., & Kryshev, I. I. (2005). Radiation conditions in Obninsk. *Atomic Energy, 99*(3), 651–657. https://doi.org/10.1007/s10512-005-0261-z

Werzi, R. (2009). The operational status of the IMS radionuclide particulate network. *Journal of Radioanalytical and Nuclear Chemistry, 282*(3), 749. https://doi.org/10.1007/s10967-009-0270-9

Werzi, R. (2010). Improving the sensitivity of radionuclide particulate monitoring stations. *Applied Radiation and Isotopes, 68*(2), 340–344. https://doi.org/10.1016/j.apradiso.2009.10.032

Winkler, P. (1973). The growth of atmospheric aerosol particles as a function of the relative humidity—II. An improved concept of mixed nuclei. *Journal of Aerosol Science, 4*(5), 373–387. https://doi.org/10.1016/0021-8502(73)90027-X

WOSMIP. (2017). WOSMIP VI: Workshop on Signatures of Man-Made Isotope Production, PNNL-26793, Pacific Northwest National Laboratory, Richland, Washington, https://wosmip.org/sites/default/files/documents/wosmipVI2017.pdf. Accessed Oct 2019

Wotawa, G., Becker, A., Kalinowski, M., Saey, P., Tuma, M., & Zähringer, M. (2010). Computation and analysis of the global distribution of the radioxenon isotope ^{133}Xe based on emissions from nuclear power plants and radioisotope production facilities and its relevance for the verification of the Nuclear-Test-Ban Treaty. *Pure and Applied Geophysics, 167*(4–5), 541–557. https://doi.org/10.1007/s00024-009-0033-0

(Received January 10, 2022, revised April 29, 2022, accepted August 17, 2022, Published online August 27, 2022)